1	Influence of Indian Ocean SST regionality on the East African Short Rains
2	
3	Weiran Liu, Kerry H. Cook, and Edward K. Vizy
4	Department of Geological Sciences, Jackson School of Geosciences, The University of Texas at
5	Austin, 1 University Station C1100, Austin, Texas, USA.
6	
7	Corresponding author: Weiran Liu
8	Email: wrliu@utexas.edu
9	
10	
11	
12	
13	
14	
15	
16	
17	
18	
19	
20	
21	Liu W, Cook KH, Vizy EK (2020) Influence of Indian Ocean SST regionality on the East
22	African Short Rains. Climate Dynamics, 10.1007/s00382-020-05265-8
23	

## Abstract

Three sub-regions of the Indian Ocean in which SSTs significantly influence the equatorial East African short rains on interannual timescales are identified, and the physical processes of this influence are studied using regional climate model simulations from the Weather Research and Forecasting model (WRF). Five 20-year ensemble integrations are generated to represent a control climate and to simulate the individual and combined effects of SSTAs in the influential regions.

SSTAs in the western Indian Ocean exert a stronger influence on the equatorial East African short rains than central and eastern Indian Ocean SSTAs both in terms of the coverage of significantly-changed precipitation and the magnitude of the precipitation response. Positive western Indian Ocean SSTAs significantly increase the short rains over 95% of the equatorial East Africa domain (30°-40°E, 5°S-5°N), while only 30% of the region responds to central and eastern Indian Ocean SSTAs. Evidence of an influential Indian Ocean dipole mode does not emerge from the analysis.

The mechanisms of this influence are diagnosed using atmospheric moisture budget and moist static energy analyses, with reference to Kelvin and Rossby wave generation as in the Gill model, but in the presence of complicated topography and nonzero background flows. Wind convergence anomalies in a moist environment primarily support precipitation anomalies in all cases, while changes in atmospheric instability are largely controlled by low-level moisture. Central and eastern Indian Ocean SSTAs change circulations and precipitation locally, but the remote influence on East Africa is weaker than that of the western Indian Ocean SSTAs.

- Key words: East African precipitation; short rains; Kenya precipitation; Indian Ocean Dipole;
- 47 interannual variability; tropical Africa rainfall; SST forcing; Greater Horn of Africa; WRF

#### 1. Introduction

The tropical East African population is dependent on rain-fed agriculture and, therefore, vulnerable to climate variation and change. The rainfall is marginal in most areas across East Africa and exhibits complicated seasonality and prominent regionality. Extreme rainfall events, both flooding and droughts, can significantly impact the agriculture, water and food security, and public health (Anyah et al. 2012; Lyon and DeWitt 2012). There are critical needs to improve our fundamental understanding of the region's precipitation, including its seasonality.

Precipitation over tropical East Africa (EA) exhibits pronounced regional variation and complicated seasonality characterized by a boreal spring "long rains" season and a boreal fall "short rains" season. Past studies (e.g., Behera et al. 2005; Ummenhofer et al. 2009) link interannual variability of the EA short rains with SST variability in the Indian Ocean. However, there are unsolved questions about the relationship between Indian Ocean SSTs and EA short rains. For example, are some regions of the Indian Ocean more influential, or do the basin-wide Indian Ocean SSTs impact EA short rains equally?

The purpose of this study is to investigate the regionality of the Indian Ocean SST forcing and the mechanisms by which this forcing influences the equatorial EA short rains in the current climatology (1998-2017). We identify hot spots of influential SSTAs, and study the hydrodynamics of the resulting perturbations in isolation and in combination using regional model (RCM) simulations. Background on the EA short rains is provided in section 2. The RCM simulations, reanalyses, observational datasets, and methodologies used are described in section 3, with a model evaluation presented in section 4. The main results are presented in section 5, and conclusions are summarized in section 6.

#### 2. Background

Rainfall in equatorial EA is often characterized by two rainy seasons. One rainy season occurs during the boreal spring, referred to as "long rains", and a second rainy season in the boreal fall is referred to as "short rains". Although the long rains provide a larger amount of rainfall to EA than the short rains (Hastenrath et al. 1993), the latter exhibit more interannual variability (Black et al. 2003; Hastenrath et al. 2011; Lyon 2014). This study, therefore, focuses on the EA short rains and associated mechanisms.

EA precipitation exhibits complex seasonality and pronounced regionality (Griffith 1972; Nicholson 1996, 1998, 2000; Herrmann and Mohr 2011; Liebmann et al. 2012; Lyon 2014). For example, Herrmann and Mohr (2011) classify the seasonality of precipitation over Africa based on multiple precipitation datasets and find equatorial Africa often exhibits two wet seasons. They suggest that the complex topography over EA and location near the equator result in the continent's richest mix of different seasonality classes. In Lyon (2014), the annual cycle of EA precipitation shows great spatial heterogeneity owing in large part to its complex terrain.

Previous studies (Hastenrath et al.1993; Black et al. 2003) relate the interannual variability of EA short rains to Pacific SSTs. However, a basinwide large-scale coupled mode, referred to as the Indian Ocean Dipole (IOD) or Indian Ocean Zonal Mode (IOZM), is found to be more influential for EA short rains than the El Niño–Southern Oscillation (ENSO) (Saji et al. 1999; Websteret al. 1999; Behera et al. 2005). For example, Bahaga et al. (2015) investigated the roles of the IOD and ENSO in the variability of EA short rains using observations and GCMs, and found that the main driver of EA short rains is the IOD and ENSO provides only a minor contribution.

EA analysis domains vary in the studies relating EA short rains to the IOD. For example, Black et al. (2003) analyze composites of extreme years using station data for 1900–97 over

(37.5°–41.25°E, 2.5°S–2.5°N) and (37.5°–41.25°E, 10°–12.5°S), and find extreme EA short rains are associated with large-scale SSTA patterns in the Indian Ocean during IOZM events. They indicate that only IOZM events that reverse the zonal SST gradient for several months trigger high rainfall. Behera et al. (2005) find that extreme years (1961, 1994, and 1997) of EA short rains over (5°S–5°N, 35°–46°E) can be explained by intrinsic zonal variability related to the IOD. Wehnhaji et al. (2018) find a strong positive correlation between October-December precipitation over (5°S–20°N, 28–52°E) and the IOD index in observational datasets, suggesting the positive-phase IOD plays a dominant role in driving EA short rains.

The correlations between the Indian Ocean SSTs and EA short rains shows interdecadal variability. Clark et al. (2003) study the rainfall during October–December along the coast in Kenya and Tanzania, and find correlations between Indian Ocean SSTs and EA precipitation in 1950-1982 and 1983-1993 nearly reverse in sign.

Several modeling studies (Ummenhofer et al. 2009; Bahaga et al. 2015) show the western Indian Ocean plays a dominant role in impacting EA short rains. Ummenhofer et al. (2009) study the relationship of October-November rainfall over (10°N–1°S, 31°–45°E) and IOD using ensemble simulations with an atmospheric general circulation model (GCM). They assess the contributions of individual (and combined) poles of the IOD to above-average precipitation over EA. They show that increased EA short rains during positive IOD are driven mainly by warming over the western Indian Ocean (38°-70°E, 12°S-12°N), leading to a reduction in sea level pressure over the western half of the Indian Ocean. Converging wind anomalies over EA lead to moisture convergence and increased convective activity.

Past regional modeling studies have shown that RCMs are able to reproduce the EA observed rainfall seasonality and regional circulation patterns (e.g., Sun et al. 1999; Segele et al.

2009; Cook and Vizy 2012; Cook and Vizy 2013; Endris et al. 2013; Ogwang et al. 2016; Han et al., 2019). The coarse resolution of current GCMs limits their capability in capturing the important regional forcing features, such as complex topography and coastlines (Cook and Vizy 2013; Endris et al. 2013; Ogwang et al. 2016). Shongwe et al. (2011) approximate the observed sensitivity of EA precipitation during October–December to Indian Ocean SSTAs, but the GCMs do not generally produce an accurate representation of the EA climate. A regional simulation with higher resolution simulations is needed because of the important role of topography in determining EA rainfall distributions (Hession and Moore 2011; Lyon 2014) and the observed complex regionality of the rainy seasons (Herrmann and Mohr 2011).

Regardless of the numerous studies discussed above, there are unsolved questions about the relationship between Indian Ocean SSTs and EA short rains. Are some regions of the Indian Ocean more influential, or do the basin-wide Indian Ocean SSTs impact EA short rains equally? In any case, what are the mechanisms of the Indian Ocean SSTs impacting EA shot rains? In this study, we will address these questions to improve our understanding of the influence of Indian Ocean SSTs on EA short rains variability.

### 3. Methodology

#### 3.1 Regional model simulations

The National Center for Atmospheric Research – National Oceanic and Atmospheric Administration Weather Research and Forecasting (WRF; Skamarock et al. 2008), version 3.8.1, is used to conduct RCM simulations over a large domain (0°-130°E, 44°S-32°N; Figure 1a) covering most of the Africa continent, and tropical and sub-tropical Indian Ocean. The simulation domain is chosen to minimize the effects of lateral boundary constraints over EA and Indian Ocean,

and to allow the development of subtropical anticyclone over the Indian Ocean. Other synoptic and large-scale circulations (e.g., the low-level Turkana jet and the overturning zonal circulation over the equatorial Indian Ocean) are also included in the simulation domain.

The model is run with 30-km horizontal resolution and 40 vertical levels, with the top of the atmosphere is set at 10 hPa. The time step is 60 seconds and model output is saved every 3 h. A combination of parameterizations is used as it has been shown to reproduce the African climate and the seasonality of EA precipitation realistically (Vizy and Cook 2009; Cook and Vizy 2012; Vizy et al.2013, 2015; Crétat et al. 2014; Han et al. 2019). Physical parameterizations selected include the Lin et al. microphysics scheme (Lin et al. 1983; Rutledge and Hobbs 1984; Chen and Sun 2002), the rapid radiative transfer model longwave radiation scheme (Mlawer et al. 1997), the Dudhia shortwave radiation scheme (Dudhia 1989), the Monin–Obukhov Similarity surface layer scheme (Skamarock et al. 2008), the Yonsei University boundary layer scheme (Hong et al. 2006), the Noah land surface model (Chen and Dudhia 2001), and Kain-Fritsch (new Eta) cumulus scheme (Kain and Fritsch 1993).

Figure 1b shows prominent topographical features over tropical East Africa as resolved in the model, which is the topography from the US Geological Survey digital elevation model interpolated to 30-km resolution. The Ethiopian highlands and the East African highlands are separated by the Turkana channel. Model elevation maxima are Mt. Kenya (37°E, 0°N) at 2783 m (~730 hPa), and the Virunga Mountains in the Rwanda-Burundi region at 1878m (~815 hPa). Lake Victoria is located between these two peaks.

Five sets of simulations, or ensembles, are run with the only difference between the ensembles being in the prescribed SSTs. One is a control climate, and four ensembles have idealized Indian Ocean SSTAs added to the control climate SSTs. The SSTAs are Gaussian-shaped

and derived from observed correlations between EA precipitation and Indian Ocean SSTs (see section 5.1). Each ensemble consists of 20 simulations that are initialized on August 1 of a different year (1998-2017), allowing the model to spin up, and run for 153 days to December 31. The simulation with 20 ensemble members is designed to suppress variability on synoptic to interannual timescales, to study the EA short rains from a climatological perspective. The model output from each 20-year run is averaged to form a climatology. Here we define a climatology as an average over the 20-year period (1998-2017) that is the focus of this study. The year 1998 is chosen as the start year to coordinate with NASA TRMM Multi-satellite Precipitation analysis (TRMM; Huffman et al. 2007) availability. Initial, lateral, and surface boundary conditions are specified at 6-hourly intervals from the European Centre for Medium-Range Weather Forecasts Interim reanalysis (ERAI; Dee et al. 2011; 1.5° latitude × 1.5° longitude) for each year (1998-2017).

In the control ensemble, climatological SSTs from ERAI averaged from 1998 to 2017 (Figure 1a) are used except for Lake Victoria (centered on 33°E, 2°S), where the daily Operational Sea Surface Temperature and Sea Ice Analysis (OSTIA; Donlon et al. 2012) values averaged from 2012 to 2017 are used. OSTIA values are available on a global 1/20° (~6 km) grid from 2007 for daily SSTs and lake surface temperatures from November 2011. OSTIA is used over Lake Victoria because it captures the observed SST gradient across Lake Victoria, while the coarser resolution (1.5°) ERAI has only one grid point over Lake Victoria. Past studies (Thiery et al. 2015; Argent et al. 2015; Woodhams et al. 2018) indicate that Lake Victoria SST gradients impact regional precipitation. In addition, ERAI SSTs are lower than OSTIA SSTs averaged over Lake Victoria by ~2 K, and they change only at monthly intervals. For these reasons, OSTIA is commonly used for regional studies of Lake Victoria and adjacent East Africa (Thiery et al. 2015; Argent et al.

2015; Woodhams et al. 2018). One disadvantage of OSTIA for our study is that the number of years of OSTIA SSTs (6 years from 2012-2017) is less than for ERAI (20 years from 1998-2017).

## 3.2 Observational/reanalysis datasets

To evaluate the accuracy of the simulated hydrodynamics, we compare with the 6-hourly ERAI reanalysis and the 6-hourly Japan Meteorological Agency's Japanese 55-Year Reanalysis (JRA-55; Kobayashi et al. 2015; 1.25° latitude × 1.25° longitude). These two reanalyses realistically capture the circulation over Africa and Indian Ocean, and are commonly used in regional studies of EA (Vizy and Cook 2012; Cook and Vizy 2013; Vizy and Cook 2019).

To evaluate precipitation in the simulations, we use TRMM at 0.25° resolution, the NOAA Precipitation Estimation from Remotely Sensed Information using an Artificial Neural Network Climate Data Record (PERSIANN; Ashouri et al. 2015; 0.25° resolution), The Climate Hazards Group Infrared Precipitation with Satellite Data (CHIRPS; Funk et al. 2015; 0.05° resolution), and The NOAA Climate Prediction Center morphing technique precipitation V2 bias-corrected dataset (CMORPH; Joyce et al. 2004; 8-km resolution).

To examine the observed correlations of Indian Ocean SSTs and EA short rains, the daily National Oceanic and Atmospheric Administration Optimum Interpolation observed SSTs (NOAA OI SST; Reynolds et al. 2007) version 2.0 at 0.25°-resolution and the monthly Hadley Centre Sea Ice and SST dataset (HadISST; Rayner et al. 2003) at 1°-resolution are used.

#### 3.3 Analysis methods

The atmospheric column moisture budget is used to connect precipitation with the largescale circulation and moisture fields. The climatological precipitation rate can be decomposed according to

210 
$$P = E + C + A + R$$
, (1)

where P is precipitation, E is evapotranspiration, E represents contributions from horizontal wind convergence in a moist environment, E is the vertically integrated horizontal advection of moisture, and E is a residual term that includes orographic precipitation, the effects of transient eddies, and numerical error (Lenters and Cook 1995; Vizy and Cook 2001; Cook and Vizy 2013).

The convergence term,  $\,C$ , which is shown to provide the strongest contribution to the total precipitation,  $\,P$ , in Section 5.3, is calculated as

$$C = -\frac{1}{g\rho_{\omega}} \int_{p_s}^{p_{top}} \left[ q\nabla_h \bullet \right] , \qquad (2)$$

where g is gravitational acceleration,  $\rho_{\infty}$  is the density of water,  $\rho_s$  and  $\rho_{top}$  are the pressure at the surface and the top of the atmosphere, respectively, q is specific humidity, and r is the horizontal wind. C is decomposed into zonal,  $C_z$ , and meridional components,  $C_m$ , as follows:

$$C_{z} = -\frac{1}{g\rho_{\omega}} \int_{\rho_{s}}^{\rho_{top}} \left( q \frac{\partial u}{\partial x} \right) dp \tag{3}$$

222 and

$$C_{m} = -\frac{1}{g\rho_{\omega}} \int_{p_{s}}^{p_{top}} \left( q \frac{\partial v}{\partial y} \right) dp . \tag{4}$$

Moist static energy (MSE) is used to measure the local instability of the atmosphere. MSE is defined as the sum of the sensible heat, latent heat, and geopotential energy contents of a parcel according to

$$MSE = c_p T + Lq + gz. (5)$$

In Eq. (5),  $c_p$  is the specific heat of air at constant pressure, T is the air temperature, L represents the latent heat of water vaporization, and z is the geopotential height. MSE profiles measure atmospheric stability and discriminate the individual roles of temperature and moisture in generating instability. MSE increases with altitude indicate a stable atmosphere, and a neutral profile generally reveals the presence of convection.

#### 4. Model Evaluation

Figures 2a-c show climatological (1998-2017) precipitation averaged over October 1 – December 15 in PERSIANN, TRMM, and the control ensemble, respectively. The primary analysis region (30°-40°E, 5°S-5°N) is shown by the black box, located over equatorial East Africa to the east of the Congo basin. As discussed below, sensitivity to domain boundaries is low. The averaging period for the short rains in the EA analysis domain is chosen as October 1-December 15, when precipitation rates in both TRMM and PERSIANN exceed 2 mm/day (Fig. 2d). The definition of the short-rains season in EA varies in the literature (Black et al. 2003; Clark et al. 2003; Yang et al. 2015; Hirons and Turner 2018). Other periods (October-November and October-December) are tested, and we find that the results are not sensitive to the choice of the short-rains averaging period in our study.

In PERSIANN, TRMM, CMORPH, and CHIRPS (Figs. 2a-d), rainfall maxima are located over Equatorial Guinea (15°E, 0°), Rwanda (28°E, 2°S). The coastal regions over East Africa (i.e., eastern Kenya and southern Somalia) and southwestern Ethiopia have higher precipitation rates than northern Kenya (35°E, 2°N) by 1-2 mm/day. The control ensemble (Fig. 2c) captures the precipitation pattern in observations, but has a wet bias over some regions, especially over the

Congo basin, consistent with past RCM studies (Vizy and Cook, 2012; Crétat et al. 2014). Precipitation in the control climatology exceeds the observed rainfall by 2-5 mm/day over the equatorial central Indian Ocean and by 5-9 mm/day over the Congo Basin. Over the EA analysis domain (black box), the control ensemble simulates precipitation patterns and magnitudes reasonably showing high rainfall rate (2-6 mm/day) over the adjacent region of Lake Victoria and low rainfall rate (<2 mm/day) over (35°-40°E, 1°-5°N), except for a wet bias over central Lake Victoria.

Figure 2d shows 11-day running means of precipitation averaged over the EA domain in PERISIANN (black), TRMM (green), CMORPH (purple), CHIRPS (orange), and the control ensemble (red). Applying the 11-day running mean effectively helps to filter out the synoptic variations. Differences between precipitation from the 20-year control simulation and the observations are insignificant at the 90% confidence level using the two-tailed Student's-t test, and the simulated seasonality is realistic. Using a threshold of 2 mm/day, the short-rains season in the control ensemble starts on October 20 and persists to December.

Figures 3a-c show climatological 850-hPa wind and specific humidity from ERAI, JRA-55, and the control ensemble, respectively. The control ensemble captures the winds in the two reanalyses, including westerlies in the equatorial Indian Ocean, northeasterlies from the Arabian Sea to Somalia, and easterlies/southeasterlies over the southern Indian Ocean between 10°S and 25°S. The model-simulated specific humidity also agrees well with ERAI and JRA-55 in terms of patterns and magnitudes. Specific humidity maxima (>12 g kg<sup>-1</sup>) are located over the Congo basin and the Maritime Continent. Other vertical levels are also examined (not shown) to conclude that the 30-km RCM provides a reasonable simulation of the 1998-2017 climatology.

Figures 3d-f show cross sections of the climatological zonal wind along the equator from ERAI, JRA-55, and the control ensemble, respectively, from 1000 to 500 hPa. Westerlies over the equatorial Indian Ocean and easterlies over the EA domain are divergent over coastal EA (eastern Kenya) in both the control ensemble and reanalyses. Low-level westerlies over the Congo basin are convergent with easterlies from the EA coast (~42°E). The westerlies over the Congo Basin in the two reanalyses (Figs. 3d and e) are located between the surface and 900 hPa, with magnitudes of 0-2 m/s. The model-simulated westerlies are stronger and deeper than in the reanalyses, extending from the surface to 750 hPa with a maxima of 5 m/s. Thus, moisture convergence (not shown) associated with the westerly flow over the Congo Basin and the easterly flow over the EA domain in the control climatology is stronger than in the reanalyses, which is consistent with the wet bias over the Congo Basin in the RCM (Figure 2c).

Moisture budget components in the control ensemble and ERAI are compared to evaluate how well the RCM captures the mechanisms of precipitation. Figures 4a-f show the P-E, A, R, C, C<sub>z</sub>, and C<sub>m</sub> terms in the moisture budget (Eqs. 1-4), respectively, in the control ensemble. P-E is positive over the Congo Basin and the Indian Ocean east of 50°E, with a maximum of 10 mm/day (Fig. 4a). Moisture advection (Fig. 4b) is negative with a magnitude below 2 mm/day, except for a region of positive values centered on (35°E, 4°N) in the Turkana Channel where southeasterly flow transports relatively wet air from the Indian Ocean (Nicholson 2016; Vizy and Cook 2019). The residual term (Fig. 4c) largely reflects topographic patterns, with strong positive values (> 8 mm/day) over the EA domain east of 35°E. Moisture convergence (Fig. 4d) with magnitudes of 2-10 mm/day is located over the Congo Basin and the EA domain to the west of Mt. Kenya (35°E), and it supports positive P-E in the same regions. Moisture divergence (Fig. 4d) is present over the

EA domain to east of 35°E. A clear east-west contrast of moisture convergence term exists over the EA domain (Fig. 4d).

Figures 4e and f show the zonal and meridional components of the moisture convergence term (Eqs. 3 and 4). Moisture convergence over the Congo Basin (Fig. 4d) is mainly supported by the zonal component (Fig. 4e) in association with westerlies over the Congo basin and easterlies from the EA coast (Fig. 3f). Moisture divergence over the EA domain east of 35°E (Fig. 4d) is primarily supported by the zonal component (Fig. 4e) and it is associated with easterlies over the EA domain and westerlies over the ocean (Fig. 3f).

It is clear from the moisture budget analysis that precipitation in the western and eastern portions of the EA domain is supported by different mechanisms, especially where the residual (Fig. 4c) and the moisture convergence terms (Fig. 4d) are concerned. The short rains over the western EA domain are mainly supported by moisture convergence while they are mainly maintained by the residual term over the eastern EA. The contribution of residual term to the precipitation over eastern EA domain indicates the possible importance of topographic effects of mountains (such as Mt. Kenya) in determining precipitation. Since it is important to average over homogenous regions, we divide the EA analysis domain into western and eastern parts separated at 35°E in the following analysis.

Figures 4g-m are the same as Figs. 4a-f but for the ERAI climatology. Similar to the control ensemble (Figs. 4a-f), ERAI indicates that the moisture convergence and residual terms have opposite signs over the western and eastern EA domains. A comparison with the simulated moisture budget (Figs. 4a-f) indicates that the control ensemble produces an accurate decomposition of the processes that maintain rainfall in the analysis domain, adding to our confidence in the regional model simulations. The simulations (Figs. 4b-e) show more structure in

the moisture budget terms along the topography (35°E) than ERAI (Figs. 4h-k) as the topography is resolved at a higher resolution in the simulations.

#### 5. Results

#### 5.1 Observed correlations of EA short rains and Indian Ocean SSTs

Figures 5a and b display correlations of TRMM rainfall averaged over the full EA domain (30°-40°E, 5°S-5°N) and Indian Ocean SSTs averaged over October 1 to December 15 in the 1998-2017 climatology using ERAI and NOAA OI SSTs, respectively. Correlations using PERSIANN (not shown) produce similar patterns. The EA short rains are positively correlated with western and central Indian Ocean SSTs along the equator, and negatively correlated with eastern Indian Ocean SSTs at approximately 5°S-10°S. The correlations are as high as 0.8 in the western and central Indian Ocean, and -0.7 in the eastern Indian Ocean. Correlations using EA short rains averaged over the western and eastern EA domains separately (not shown) produce similar patterns over the western, central, and eastern Indian Ocean.

To understand the extent to which the three SSTAs occur independently, correlations between SSTs averaged over the black boxes in Figure 5 are calculated. Results using NOAA OI SST, ERAI SST, and HadISST are similar. The western and eastern Indian Ocean SSTAs are not significantly correlated at the 90% confidence level, with a correlation coefficient of -0.24. SSTAs in the western and eastern Indian Ocean have opposite signs in 11 (55%) out of 20 years from 1998 – 2017. In contrast, SSTAs in the western and central Indian Ocean are highly correlated (>99% confidence level) with a correlation of 0.92.

Past studies (e.g., Saji et al. 1999; Li et al. 2003; Saji et al. 2003; Luo et al. 2010) report a dipole mode of SST variability in the tropical Indian Ocean (IOD), quantified by the SST

difference between the tropical western Indian Ocean (50-70°E, 10°S-10°N) and the tropical southeastern Indian Ocean (90°-110°E, 10°S-0°), referred to as the IOD index. The averaging regions used in calculating the IOD index are different from the regions identified here as being especially influential for the EA short rains in Figure 5. Further, our results suggest that the western and eastern Indian Ocean SSTAs are not significantly anticorrelated using the averaging boxes in Figure 5 for 1998-2017. Other studies (Nicholls and Drosdowsky 2001; Dommenget and Latif 2002; Zhao and Nigam, 2015; Wang et al. 2019) find a similar lack of anticorrelation using the averaging regions defined for the IOD index. The fundamental mechanisms of the IOD are beyond the purpose of this study and not discussed further.

Figure 5c shows the locations and magnitudes of the idealized SSTAs used in the perturbation ensemble simulations. The choice of these SSTAs is guided by the correlations shown in Figs. 5a and b. In addition to the western, central, and eastern Indian Ocean, significant correlations also exist over (65°-70°E, 8°-12°N) in the Arabian Sea in Figs. 5a and b. However, we do not apply SSTAs over the Arabian Sea in the perturbation simulations because the correlations are less robust in the sense that they are sensitive to the exact choices of EA averaging region.

The three SSTAs shown in Figure 5c are Gaussian in shape and have maximum amplitude of +1K in the western and central Indian Ocean, and -1K in the eastern Indian Ocean, covering the regions with significant correlations shown in Figs. 5a and b. The SSTA maximum amplitudes are larger than the standard deviations of the SSTAs in ERAI (0.3-0.4K) to produce diagnosable responses, but similar in magnitude to those of the most extreme years.

Table 1 provides a reference for naming the five ensemble simulations. The three SSTAs in Fig. 5c are imposed individually in the WIO, CIO, and EIO ensembles. The ALL ensemble

includes all three SSTAs shown in Fig. 5c, comparing with the linear superposition of the WIO, CIO, and EIO ensembles to evaluate the potential for interference among the individually-forced responses.

## 5.2 Precipitation anomaly in perturbation ensembles

Figures 6a, b, c and d show anomalous precipitation, defined as differences from the CTL climatology, for the WIO, CIO, EIO, and ALL climatologies (see Table 1). Only areas with confidence levels higher than 90% are shaded. The same precipitation anomalies are shown in Figures 6e, f, g, and h, but enlarged to focus on the EA domain and adjacent regions. The percentages of the grid boxes in the EA domain that are associated with significantly-changed precipitation is indicated in the upper left of each panel.

Precipitation anomalies associated with a warm western Indian Ocean (Fig. 6a) cover a large region of tropical EA (22°-41°E, 10°S-8°N), with decreased precipitation in the Arabian Sea (60°-80°E, 6°-15°N) and the south Indian Ocean (80°-100°E, 7°-16°S). 95% of the grid points in the EA analysis domain have significantly-increased precipitation (0-4 mm/day) due to the warm western Indian Ocean (Fig. 6e). Eastern Kenya, southern Somalia, and southern Ethiopia also show significantly-increased precipitation (1-2 mm/day).

In the CIO simulation, precipitation increases over the imposed SSTA as in the WIO simulation, and there is decreased precipitation over the western and eastern Indian Ocean near the equator (Fig. 6b). The dry region in the western Indian Ocean extends onto the African coast (southern Somalia), and precipitation responses are not homogeneous over the EA domain (Fig. 6f). The northeastern quadrant (29% of the EA domain) becomes significantly drier due to the

warm central Indian Ocean SSTA forcing, while regions west of 38°E (8% of the EA domain) become significantly wetter by 0-2 mm/day.

When cool SSTAs are imposed in the eastern Indian Ocean in the EIO ensemble (Fig. 6c), precipitation decreases over the SSTAs, and increases over the western equatorial Indian Ocean (40°-70°E, 0°-8°S) and to the north of the cold anomaly (80°-110°E, 0°-5°N). 30% of the EA domain shows significantly increased precipitation (Fig. 6g).

Comparing the precipitation responses in the three simulations, the percentages of the grid boxes in the EA domain that are associated with significantly-changed precipitation in the WIO ensemble are about three times those in the CIO and EIO ensembles.

ALL simulations are significantly wetter over the western and central IO, and the EA (22°-55°E, 10°S-10°N), including Kenya, Somalia, Ethiopia, and Uganda (Fig. 6d), and drier over the southeastern IO and the Bay of Bengal than the control simulations. 92% of the grid points in the EA analysis domain have significantly-increased precipitation (Fig. 6h), similar to the WIO simulations (Fig. 6e).

Since the precipitation anomalies shown in Figure 6 are averaged over two and a half months, they could represent changes in magnitudes, or/and changes in the timing of the onset or demise of the rainy season. Figure 7a shows the 11-day running mean of precipitation averaged over the western EA domain (30°-35°E, 5°S-5°N) in the CTL (black), WIO (dark blue), CIO (light blue), EIO (pink), and ALL (red) climatologies, along with the linear superposition of the WIO, CIO, and EIO ensembles (green). The WIO ensemble (dark blue line) shows significantly (>90% confidence level) increased precipitation compared with the CTL ensemble (black line) with a maximum of 9 mm/day on November 11.

The CIO (light blue line) and EIO (pink line) simulations also show increased rainfall compared with the CTL ensemble but in smaller magnitudes than for the WIO ensemble. Precipitation anomalies are up to 1.1 mm/day in the CIO ensemble and 0.8 mm/day in the EIO ensemble. However, the CIO and EIO simulations do not produce significant (90% confidence level) changes of precipitation from the control climatology during the short rain season. The precipitation changes are significant only on specific dates rather than over the entire period like for WIO.

The response of EA precipitation to the imposition of all three SSTAs together (the ALL ensemble; red line) does not equal the sum of the responses to the SSTAs individually (green line). When multiple SSTAs are applied, nonlinearities are introduced. The maximum precipitation anomaly in ALL is smaller than the superposition by 1.5 mm/day. The daily evolution of precipitation in the ALL simulation is more similar to the WIO simulation in magnitude than to the superposition of the three SSTAs. Although the ALL ensemble changes the large-scale zonal gradient of Indian Ocean SSTs, the response of EA precipitation is not significantly different from the WIO ensemble.

Figure 7b shows the 11-day running means of precipitation averaged over the eastern EA domain (35°-40°E, 5°S-5°N) in multiple simulations similar to Fig. 7a. Eastern-domain precipitation anomalies in the perturbation simulations are similar to those in the western EA domain (Fig. 7a) but with smaller magnitudes. The statistical significance of the precipitation responses in the different ensembles are also similar to those in the west (Fig. 7a), with significantly-increased short rain precipitation in the WIO ensemble and insignificantly increased precipitation in the CIO and EIO.

Both Figures 6 and 7 indicate that western Indian Ocean SSTAs exert a stronger influence on EA short rains than central and eastern Indian Ocean SSTAs. The central and eastern Indian Ocean SSTAs produce significantly-changed precipitation over some regions of the tropical Indian Ocean, but their influence on African precipitation in boreal fall is less than the western Indian Ocean SSTAs.

## 5.3 Mechanisms of the Indian Ocean SSTs impacting the EA short rains

To connect precipitation responses in the WIO simulations to circulations, Figure 8 depicts anomalies from the CTL ensemble in the components of the atmospheric moisture budget [Eq. (1)] for the WIO simulations. Positive P-E anomalies (Fig. 8a) exist over the Congo Basin, the EA analysis domain, and the western Indian Ocean. Evaporation anomalies (not shown) are not influential to precipitation anomalies with magnitudes less than 1 mm/day. The magnitudes of A anomalies (Fig. 8b) are generally under 1 mm/day, except for 2-3 mm/day near the Turkana Channel. The anomalies of the residual term (Fig. 8c) show structures along the topography. The increased P-E (Fig. 8a) extending from the Congo basin to the western Indian Ocean is not explained by A (Fig. 8b) and R anomalies (Fig. 8c).

Figure 8d shows the difference in moisture convergence term [Eq. (2)] between the WIO and CTL simulations, representing the convergence of wind perturbation in a moist environment, along with anomalous winds at 850 hPa. Winds at 850 hPa are characteristic to represent low levels (975-700 hPa; not shown). The anomaly of C term most closely resembles P-E anomaly (Fig. 8a). Anomalous wind convergence is found over equatorial Africa on the east of  $20^{\circ}E$  and the western Indian Ocean. The warm western Indian Ocean SSTAs strengthen the wind convergence in a moist environment over the western EA domain in the CTL (Fig. 4d) and weaken the wind

divergence over the eastern EA domain (Fig. 4d). The anomalous 850-hPa winds (Fig. 8d) are mainly zonal from the Congo basin to the western EA domain while they are more meridional along the African coast (Somalia and eastern Tanzania).

Figures 8e and f show zonal [Eq. (3)] and meridional [Eq. (4)] components of C anomaly, respectively, along with the same anomalous winds as Fig. 8d. Patterns of both components indicate complicated heterogeneity. Both the eastern and western parts of the EA domain show positive P-E anomalies due to the warm western Indian Ocean SSTAs (Fig. 8a), but they are controlled by different components of C anomaly. Specifically, 70% of anomalous P-E (Fig. 8a) over the western EA domain is supported by Cz (Fig. 8e). Over the eastern EA domain, 125% of the anomalous P-E (Fig. 8a) is supported by Cm (Fig. 8f) but it is suppressed by R term (Fig. 8c). The meridional winds from southern and northern hemispheres are convergent on the equator near the coast over southern Somalia and eastern Kenya (Fig. 8f), associated with positive Cm anomalies over the eastern EA domain. The westerlies from the Congo basin proceed to the northern and southern sides of Mt. Kenya, associated with negative Cm anomalies over (30°-34°E, 1°S-5°N) (Fig. 8f).

To understand the changes of low-level winds in large-scale circulation, Figure 9 shows anomalous geopotential heights and winds at 850 hPa in the WIO ensemble. Geopotential height anomalies and wind anomalies show patterns similar to the response to steady thermal forcing on the equator from the shallow water equations (Gill 1980). The western Indian Ocean heating generates negative geopotential height anomalies in the tropical Indian Ocean between 10°N and 10°S and the western Indian Ocean, over which the geopotential height anomalies are not centered exactly on the equator but in the southern hemisphere. A possible explanation for this asymmetry is that land north of the equator (e.g., the Horn of Africa) extends to the east and the western Indian

Ocean SSTAs (SSTA1 in Fig. 5c) spatially cover a greater area south of the equator, hence, the SST forcing is weighted more towards the southern hemisphere. Positive geopotential height anomalies (0-4 gpm) are found over India, southeastern Asia, and the southern Indian Ocean centered at (75°E, 14°S).

Anomalous zonal flow is confined near the equator ( $10^{\circ}\text{S}-10^{\circ}\text{N}$ ), consistent with Gill (1980). Considering the generations of the Rossby and Kelvin waves in Gill (1980), the Kelvin wave to the east of the western Indian Ocean heating maximum (yellow dot) produces anomalous zonal flow into the heating close to the equator (Fig. 9) across the equatorial Indian Ocean. The equatorial zonal flow to the west of the heating are weaker than to the east, different from the classic Gill type responses (1980), possibly due to the influence of the highlands over East Africa and Ethiopia (up to 700 hPa). The anomalous westerlies/southwesterlies over the Turkana Channel (Fig. 9) are associated with the negative A anomalies over the same region (Fig. 8b). Rossby wave response occurs to the west of western Indian Ocean heating. The presence of the Rossby mode is indicated by the cyclonic anomaly over ( $35^{\circ}-55^{\circ}\text{E}$ ,  $0^{\circ}-15^{\circ}\text{S}$ ) and meridional wind perturbations over ( $40^{\circ}-50^{\circ}\text{E}$ ,  $0^{\circ}-15^{\circ}\text{N}$ ), associated with the equatorward wind perturbations and the positive Cm anomalies over the coast (Fig. 8f).

The classic Gill model (Gill 1980) assumes a quiescent basic state while the basic-state flow is non-zero in our case. Considering the basic-state flows in the control simulations (Figs. 3c and f), the western Indian Ocean heating weakens the equatorial westerlies over the Indian Ocean and the southeasterlies over the Turkana Channel by producing zonal flows in the Kelvin wave response, and strengthens the equatorward flows over the African coast (Somalia and eastern Tanzania) associated with the meridional perturbations in the Rossby wave.

To connect precipitation responses in the CIO simulations to circulations, Figure 10 shows the CIO minus CTL differences in P-E, C, Cz, and Cm terms in the moisture budget. Vectors in Figs. 10d-f are anomalous winds at 850 hPa for the CIO ensemble average. Unlike the WIO simulations, the anomalous P-E in CIO simulations is inhomogeneous with positive P-E anomaly over the western EA domain, and negative P-E anomaly over the eastern EA domain and the western Indian Ocean. The magnitudes of P-E over the continent (< 1 mm/day) in the CIO simulations are smaller than the WIO simulations (1-6 mm/day). The anomalous A and A terms (not shown) are not influential to the patterns of A0 monalies, similar to Figs. 8b and c.

The pattern of the anomalous C term (Fig. 10d) resembles P-E anomalies (Fig. 10a), similar to WIO simulations, except for structures along the topography near 35°E. The negative P-E anomaly over the eastern EA domain and the ocean (Fig. 10a) is dominated by zonal wind divergence (Fig. 10c), associated with offshore wind anomalies. Positive Cm anomalies (Fig. 10d) are found over Somalia, northern Kenya, and Tanzania, associated with meridional wind convergence, but the magnitudes of Cm anomalies are smaller than Cz (Fig. 10c) by approximately 0.3 mm/day.

Figure 11 shows differences in geopotential heights and winds at 850 hPa between the CIO and CTL simulations. Similar to the classic Gill model, anomalous westerlies near the equator (5°S-5°N) occur on the west of central Indian Ocean SSTAs and anomalous easterlies exist on the east of central Indian Ocean SSTAs in the presence of Kelvin wave. These anomalous equatorial zonal flows are associated with anomalous zonal wind convergence in a moist environment over the central Indian Ocean (not shown) and, therefore, the significantly-increased precipitation (Fig. 6b). The anomalous westerlies from the African continent to the central Indian Ocean heating are

associated with a strengthening of the offshore low-level flow over equatorial East Africa in the CTL (Fig. 4c), associated with the negative Cz anomalies near the coast (Fig. 10c). There are two cyclonic anomalies centered at (65°E, 15°S) and (65°E, 8°N) on the southwest and northwest of the central Indian Ocean SSTA maximum (yellow dot) in the presence of Rossby wave. Poleward wind anomalies over 75°- 85°E in both hemispheres are meridional perturbations of Rossby wave. The return flows of the Rossby wave response are the equatorward flows over the African coast, associated with the positive Cm anomalies over Somalia, northern Kenya, and Tanzania (Fig. 10d).

Figure 12 shows the EIO minus CTL differences in P-E, C, Cz, and Cm terms in the moisture budget. Anomalous P-E (Fig. 12a) increases by 0-1 mm/day over the EA domain, which is much less than in the WIO simulations. Again, the anomalous C term (Fig. 12b) resembles the anomalous P-E term (Fig. 12a) with changes in Cz (Fig. 12c) mostly responsible for the positive anomalies while being slightly offset by Cm (Fig. 12d) as there is anomalous low-level easterly flow from the Indian Ocean into the equatorial East Africa. That being said, the anomalous flow is weaker in magnitude for EIO compared to the WIO and CIO cases.

Figure 13 shows 850-hPa geopotential height and wind anomalies for the EIO ensemble. The anomalous low-level height response is asymmetric about the equator as the center of the SSTAs is located more off the equator (10°S) for EIO compared to the WIO and CIO cases. There is a Gill-like anomalous anticyclonic anomaly pattern to the west of eastern Indian Ocean SSTAs with the stronger height anomalies in the southern hemisphere. Along the equator, the anomalous flow is easterly, indicating a weakening of the low-level equatorial westerly flow across the basin (Fig. 3c). While the anomalous equatorial zonal flow is still easterly to the west of 55°E, it is much

weaker than over the eastern half of the Indian Ocean basin as the SST forcing is much further away compared to the other cases.

To compare changes in the instability of the atmosphere due to different SSTAs, Figure 14 displays anomalous MSE (black),  $c_pT$  (green), and Lq (red) [Eq. (5)] averaged over the western (solid) and eastern EA domains (dashed) in the WIO, CIO, and EIO simulations. Note the gz component anomalies are minimal, and thus are not shown in Fig. 14. MSE in the CTL simulation average (not shown) decreases from surface to 600 hPa over both western and eastern EA domains indicating the low-level atmosphere is unstable.

For WIO (Fig. 14a), anomalous low-level MSE (black line) has a negative slope over both domains but at different levels. For example, increases in atmospheric instability over the western domain (black solid line) occur between 925 and 700 hPa, but occur between 1000 and 850 hPa over the eastern EA domain (black dashed line). Clearly, the elevation differences between these two regions has a considerable impact (Fig. 1b). Changes in the vertical MSE profiles over both domains (black line) are primarily associated with changes in Lq (red line). Low-level atmospheric moisture content is enhanced due to the warm western Indian Ocean SSTAs and thus leads to a destabilization of the low-level atmosphere.

For CIO (Fig. 14b), the vertical profile of anomalous MSE is neutral over the western EA domain (black solid line), but the atmosphere between 900 and 700 hPa is more stable over the eastern EA domain (black dashed line), consistent with the wetter west region and drier east region rainfall pattern in Fig. 6f. Anomalous MSE (black line) is dominated by changes in *Lq* (red line) over both domains as the low-level moisture (surface to 800 hPa) increases over the western EA domain, and decreases over the eastern EA domain.

For EIO (Figure 14c), changes in  $c_pT$  are approximately zero indicating minimal temperature changes over the two EA domains. The MSE profile is, therefore, supported by changes in Lq. Anomalous Lq (red line) is positive from the surface to 400 hPa indicating enhanced atmospheric moisture. The eastern Indian Ocean SSTAs increase atmospheric moisture, but only generate a neutral vertical profile of MSE (black line), less influential than the western SSTAs (Fig. 14).

Changes in vertical speeds over the EA domain and the Indian Ocean for the different simulations are also investigated. Results from this analysis (not shown) show that the warm western Indian Ocean SSTAs are associated with the strongest anomalous upward vertical motions over the EA domain, indicating a weakening of the subsidence near the EA coast. Central and eastern Indian Ocean SSTAs induce anomalous vertical motions over the ocean, but their influence on the EA subsidence is minor.

#### 6. Summary and conclusions

The boreal fall short rains over equatorial East Africa (30°-40°E, 5°S-5°N) exhibit considerable interannual variability and regionality over the complex topography (Black et al. 2003; Hastenrath et al. 2011; Lyon 2014). Past studies (e.g., Behera et al. 2005; Ummenhofer 2009) associate this interannual variability with SST variations in the Indian Ocean. Our purpose is to identify which regions of the Indian Ocean most strongly influence the boreal fall equatorial East African short rains on interannual timescales, and to investigate the physical mechanisms responsible.

Three "hot spot" regions are identified, located on or near the equator in the western, central, and eastern Indian Ocean. A regional climate model (WRF) with 30-km horizontal resolution is

used to conduct 5 sets of simulations in which 20-member ensembles represent a control climate and climates with idealized SSTAs. The control simulations use climatological (1998-2017) SSTs. In the idealized simulations, various Gaussian-shaped SSTAs derived from observed correlations between East African precipitation and Indian Ocean SSTs are imposed (Fig. 5c). One additional ensemble includes all three SSTAs to evaluate the potential for interference among the individually-forced responses.

The results are summarized as follows:

- The control simulations capture the observed patterns and seasonality of East African precipitation (Fig. 2) and circulation (Fig. 3) with reasonable accuracy, albeit with a wet bias over the Congo basin. The simulated processes that support regional rainfall as revealed by the atmospheric moisture budget also agree well with reanalyses. This analysis shows that the mechanisms that support precipitation in the western and eastern parts of the equatorial East Africa analysis domain are fundamentally different due to the presence of complex topography (Fig. 4). The short rains over the western half of the domain are mainly supported by wind convergence in a moist environment, while orographic uplift plays a dominant role farther east.
- Short rains over the analysis domain are positively correlated with western and central Indian Ocean SSTs, and negatively correlated with eastern Indian Ocean SSTs in observations from 1998-2017 (Fig. 5). The western and eastern Indian Ocean SSTAs are not significantly anti-correlated at the 90% confidence level, consistent with some past studies that also reveal an absence of the Indian Ocean Dipole as a coherent mode of variability (Nicholls and Drosdowsky 2001; Dommenget and Latif 2002; Zhao and Nigam, 2015; Wang et al. 2019).

SSTAs in the western Indian Ocean are shown to exert a stronger influence on the equatorial East African short rains than central and eastern SSTAs in terms of both the coverage of significantly-changed precipitation (Fig. 6) and the magnitude of the precipitation response (Fig. 7), consistent with past studies (Ummenhofer et al. 2009; Bahaga et al. 2015). Specifically, western Indian Ocean SSTAs produce significantly enhanced precipitation over 95% of the analysis domain, while only 30% of the region responds to central and eastern Indian Ocean SSTAs (Fig. 6). The maximum precipitation anomaly associated with western Indian Ocean SSTAs is about three times larger than the anomalies due to central and eastern SSTAs in the simulation (Fig. 7). The response of the precipitation field to the three SSTAs together does not equal the sum of the responses to the SSTAs individually indicating the presence of nonlinearity (Fig. 7).

- The atmospheric moisture budget analysis shows that the anomalous wind convergence closely resembles the precipitation anomaly in all cases (Figs. 8, 10, and 12). The patterns of geopotential heights and winds anomalies caused by positive western and central Indian Ocean SSTAs are similar to the Gill response (1980) to steady heating on the equator (Figs. 9 and 11), while the simulations with negative eastern Indian Ocean SSTAs are similar to the off-equator cooling case (Fig. 13). The main differences between the classic Gill response (1980) and our cases are due to the presence of complex topography (especially in the simulations with western Indian Ocean SSTAs) and background flows.
- The increased precipitation over the western domain due to western Indian Ocean SSTAs is mainly supported by zonal wind convergence anomalies, associated with anomalous westerlies from the Congo basin in the Kelvin wave response. The meridional wind

convergence anomaly contributes to increased precipitation over the eastern domain most strongly, in association with the meridional perturbations of the Rossby wave (Fig. 8).

The vertical profiles of anomalous MSE are dominated by the moisture component in all three cases (Fig. 14). The increases in low-level moisture that accompany western Indian Ocean warming destabilize the low-level atmosphere over equatorial East Africa. SSTAs in the central and eastern Indian Ocean also modify the region's atmospheric moisture, but they are less influential than western Indian Ocean SSTAs in changing atmospheric instability.

This study shows that western Indian Ocean SSTAs are much more influential for perturbing the equatorial East African short rains on interannual time scales than SSTAs elsewhere in the Indian Ocean. In particular, we find no evidence of connections between an Indian Ocean dipole mode and equatorial East African rainfall. The mechanisms of the forcing from the western Indian Ocean are related to the shallow-water Gill model (1980), but in the presence of complicated topography and nonzero background flows. East African rainfall, including its supporting mechanisms, is highly regional, encouraging caution when choosing averaging regions in future studies of precipitation variability on all time scales. Our study designed the idealized SSTAs based on the correlations of the East African short rains and Indian Ocean SSTs in the current climatology (1998-2017). The next step is to consider the decadal and multi-decadal variability of this correlation and investigate the relationship of Indian Ocean SSTs and East African short rains over a longer time period to better understand the robustness of the results presented here.

## Acknowledgements

This work was funded by NSF Award #1701520. The authors acknowledge the Texas Advanced Computing Center (TACC) at The University of Texas at Austin for providing HPC and database resources that have contributed to the research results reported within this paper. URL: <a href="http://www.tacc.utexas.edu">http://www.tacc.utexas.edu</a>. The Grid Analysis and Display System software (GrADS) developed at COLA/IGES was used for generating the figures.

# References

663	Anyah RO, Qiu W (2012) Characteristic 20th and 21st century precipitation and temperature
664	patterns and changes over the Greater Horn of Africa. Int J Climatol 32(3), 347-363. doi:
665	10.1002/joc.2270
666	Argent R, Sun X, Semazzi F, Xie L, Liu B (2015) The development of a customization framework
667	for the WRF Model over the Lake Victoria basin, Eastern Africa on seasonal
668	timescales. Advances in Meteorol. doi: 10.1155/2015/653473
669	Ashouri H, Hsu KL, Sorooshian S, Braithwaite DK, Knapp KR, Cecil LD, Nelson BR, Prat OP
670	(2015) PERSIANN-CDR: Daily precipitation climate data record from multisatellite
671	observations for hydrological and climate studies. Bull Am Meteorol Soc 96(1), 69-83. doi
672	10.1175/BAMS-D-13-00068.1
673	Bahaga TK, Mengistu Tsidu G, Kucharski F, Diro GT (2015). Potential predictability of the sea-
674	surface temperature forced equatorial East African short rains interannual variability in the
675	20th century. Q J Roy Meteorol Soc141(686), 16-26. doi: 10.1002/qj.2338
676	Behera SK, Luo JJ, Masson S, Delecluse P, Gualdi S, Navarra A, Yamagata T (2005) Paramount
677	impact of the Indian Ocean dipole on the EA short rains: A CGCM study. J Clim 18(21),
678	4514-4530. doi: 10.1175/JCLI3541.1
679	Black E, Slingo J, Sperber KR (2003) An observational study of the relationship between
680	excessively strong short rains in coastal East Africa and Indian Ocean SST. Mon Weather
681	Rev 131(1), 74-94. doi: 10.1175/1520-0493(2003)131<0074:AOSOTR>2.0.CO;2
682	Crétat J, Vizy EK, Cook KH (2014) How well are daily intense rainfall events captured by current
683	climate models over Africa?. Clim Dyn 42(9-10), 2691-2711. doi: 10.1007/s00382-013-
684	1796-7

685 Chen F, Dudhia J (2001) Coupling an advanced land surface-hydrology model with the Penn State–NCAR MM5 modeling system. Part I: Model implementation and sensitivity. Mon 686 Weather Rev 129, 569–585, doi:10.1175/1520-0493(2001)129,0569:CAALSH.2.0.CO;2. 687 Chen SH, Sun WY (2002) A one-dimensional time dependent cloud model. J Meteor Soc Japan 688 80, 99–118, doi:10.2151/jmsj.80.99. 689 Clark CO, Webster PJ, Cole JE (2003) Interdecadal variability of the relationship between the 690 Indian Ocean zonal mode and EA coastal rainfall anomalies. J Clim 16(3), 548-554. doi: 691 10.1175/1520-0442(2003)016<0548:IVOTRB>2.0.CO;2 692 693 Cook KH, Vizy EK (2012) Impact of climate change on mid-twenty-first century growing seasons in Africa. Clim Dyn 39, 2937–2955, doi:10.1007/s00382-012-1324-1. 694 Cook KH, Vizy EK (2013) Projected changes in EA rainy seasons. J Clim 26(16), 5931-5948. doi: 695 10.1175/JCLI-D-12-00455.1 696 Dee DP, Uppala SM, et al (2011) The ERA-Interim reanalysis: Configuration and performance of 697 the data assimilation system. Q J Roy Meteorol Soc 137(656), 553-597. doi: 698 10.1002/qj.828 699 Dommenget D, Latif M (2002) A cautionary note on the interpretation of EOFs. J Clim 15(2), 216-700 225. doi: 10.1175/1520-0442(2002)015<0216:ACNOTI>2.0.CO;2 701 Donlon CJ, Martin M, Stark J, Roberts-Jones J, Fiedler E, Wimmer W (2012) The operational sea 702 surface temperature and sea ice analysis (OSTIA) system. Remote Sensing of 703 704 Environment 116, 140-158. doi: 10.1016/j.rse.2010.10.017 Dudhia J (1989) Numerical study of convection observed during the winter monsoon experiment 705 using a mesoscale two dimensional model. J Atmos Sci 46, 3077–3107, doi:10.1175/1520-706 707 0469(1989)046,3077:NSOCOD.2.0.CO;2.

708	Endris HS, Omondi P, et al (2013) Assessment of the performance of CORDEX regional climate
709	models in simulating East African rainfall. J Clim 26(21), 8453-8475. doi: 10.1175/JCLI-
710	D-12-00708.1
711	Funk C, Peterson P, Landsfeld M, Pedreros D, Verdin J, Shukla S, Husak G, Rowland J, Harrison
712	L, Hoell A, Michaelsen J (2015) The climate hazards infrared precipitation with stations—
713	a new environmental record for monitoring extremes. Sci Data 2:150066. doi:
714	10.1038/sdata.2015.66
715	Gill AE (1980) Some simple solutions for heat-induced tropical circulation. Q J Roy Meteorol Soc
716	106(449), 447-462. doi: 10.1002/qj.49710644905
717	Han F, Cook KH, Vizy EK (2019) Changes in intense rainfall events and dry periods across Africa
718	in the twenty-first century. Clim Dyn 1-21. doi: 10.1007/s00382-019-04653-z
719	Hastenrath S, Nicklis A, Greischar L (1993) Atmospheric-hydrospheric mechanisms of climate
720	anomalies in the western equatorial Indian Ocean. J Geophs Res: Oceans 98(C11), 20219-
721	20235. doi: 10.1029/93JC02330
722	Hastenrath S, Polzin D, Mutai C (2011) Circulation mechanisms of Kenya rainfall anomalies. J
723	Clim 24(2), 404-412. doi: 10.1175/2010JCLI3599.1
724	Herrmann SM, Mohr KI (2011) A continental-scale classification of rainfall seasonality regimes
725	in Africa based on gridded precipitation and land surface temperature products. J Appl
726	Meteorol 50(12), 2504-2513. doi: 10.1175/JAMC-D-11-024.1
727	Hession SL, Moore N (2011) A spatial regression analysis of the influence of topography on
728	monthly rainfall in East Africa. Int J Climatol 31(10), 1440-1456. doi: 10.1002/joc.2174

729 Hirons L, Turner A (2018) The impact of Indian Ocean mean-state biases in climate models on the representation of the East African short rains. J Clim 31(16), 6611-6631. doi: 730 10.1175/JCLI-D-17-0804.1 731 732 Hong SY, Noh Y, Dudhia J (2006): A new vertical diffusion package with an explicit treatment of entrainment processes. Mon Weather Rev 134, 2318–2341, doi:10.1175/MWR3199.1. 733 Huffman GJ, Bolvin DT, Nelkin EJ et al (2007) The TRMM multisatellite precipitation analysis 734 (TMPA): Quasi-global, multiyear, combined-sensor precipitation estimates at fine scales. J 735 Hydrometeorol 8(1), 38-55. doi: 10.1175/JHM560.1 736 Joyce RJ, Janowiak JE, Arkin PA, Xie P (2004) CMORPH: a method that produces global 737 precipitation estimates from passive microwave and infrared data at high spatial and 738 resolution. J Hydrometeorol 5:487-503. doi: 739 temporal 10.1175/1525-7541(2004)005<0487:CAMTPG>2.0.CO;2 740 Kain JS, Fritsch JM (1993) Convective parameterization for mesoscale models: The Kain–Fritsch 741 scheme. The Representation of Cumulus Convection in Numerical Models, Meteor 742 Monogr No. 46, Amer Meteor Soc 165–170. doi: 10.1007/978-1-935704-13-3 16 743 Kobayashi S, Ota Y, Harada Y, Ebita A, Moriya M, Onoda H, Onogi K, Kamahori H, Kobayashi 744 C, Endo H, Miyaoka K, Takahashi K (2015) The JRA-55 reanalysis: General specifications 745 and basic characteristics. J Meteorol Soc Jpn Ser. II 93(1), 5-48. doi: 10.2151/jmsj.2015-746 001 747 748 Lenters JD, Cook KH (1995) Simulation and diagnosis of the regional summertime precipitation climatology of South America. J Clim 8(12), 2988-3005. doi: 10.1175/1520-749 0442(1995)008<2988:SADOTR>2.0.CO;2 750

- Liebmann B, Bladé I, et al (2012) Seasonality of African precipitation from 1996 to 2009. J Clim
- 752 25(12), 4304-4322. doi: 10.1175/JCLI-D-11-00157.1
- Lin YL, Farley RD, Orville HD (1983) Bulk parameterization of the snow field in a cloud model. J
- 754 Clim Appl Meteorol 22(6), 1065-1092. doi: 10.1175/1520-
- 755 0450(1983)022<1065:BPOTSF>2.0.CO;2
- Luo JJ, Zhang R, Behera SK, Masumoto Y, Jin FF, Lukas R, Yamagata T (2010) Interaction
- between El Nino and extreme Indian ocean dipole. J Clim 23(3), 726-742. doi:
- 758 10.1175/2009JCLI3104.1
- Lyon B (2014) Seasonal drought in the Greater Horn of Africa and its recent increase during the
- 760 March–May long rains. J Clim 27(21), 7953-7975.
- Lyon B, DeWitt DG (2012) A recent and abrupt decline in the East African long rains. Geophys
- 762 Res Lett 39(2). doi: 10.1029/2011GL050337
- 763 Mlawer EJ, Taubman SJ, Brown PD, Iacono MJ, Clough SA (1997) Radiative transfer for
- inhomogeneous atmospheres: RRTM, a validated correlated-k model for the longwave. J
- 765 Geophys Res 102, 16 663–16 682, doi:10.1029/97JD00237.
- 766 Nicholson SE (2016) An analysis of recent rainfall conditions in eastern Africa. Int J
- 767 Climatol 36(1), 526-532. doi: 10.1002/joc.4358
- Nicholls N, Drosdowsky W (2001) Is there an equatorial Indian Ocean SST Dipole, independent
- of the El Nino Southern Oscillation. Preprints. In Symp. on Climate Variability, the Oceans,
- and Societal Impacts (pp. 17-18). [Available online
- at https://ams.confex.com/ams/annual2001/techprogram/paper 17337.htm.]

772 Ogwang BA, Chen H, Li X, Gao C (2016) Evaluation of the capability of RegCM4. 0 in simulating East African climate. Theoretical and applied climatology 124(1-2), 303-313. doi: 773 10.1007/s00704-015-1420-3 774 775 Rayner NAA, Parker DE, et al (2003) Global analyses of sea surface temperature, sea ice, and night marine air temperature since the late nineteenth century. J Geophys Res: 776 Atmos 108(D14). doi: 10.1029/2002JD002670 777 Reynolds RW, Smith TM, Liu C, Chelton DB, Casey KS, Schlax MG (2007) Daily high-778 resolution-blended analyses for sea surface temperature. J Clim 20(22), 5473-5496. doi: 779 780 10.1175/2007JCLI1824.1 Rutledge SA, Hobbs PV (1984) The mesoscale and microscale structure and organization of clouds 781 and precipitation in midlatitude cyclones. XII: A diagnostic modeling study of precipitation 782 development in narrow cold-frontal rainbands. J Atmos Sci 41(20), 2949-2972. doi: 783 10.1175/1520-0469(1984)041<2949:TMAMSA>2.0.CO;2 784 Saji NH, Goswami BN, Vinayachandran PN, Yamagata T (1999) A dipole mode in the tropical 785 Indian Ocean. Nature 401(6751), 360. doi: 10.1038/43854 786 Saji NH, Yamagata T (2003) Possible impacts of Indian Ocean dipole mode events on global 787 788 climate. Clim Res 25(2), 151-169. doi: 10.3354/cr025151 789 Segele ZT, Lamb PJ, Leslie LM (2009) Large-scale atmospheric circulation and global sea surface temperature associations with Horn of Africa June–September rainfall. Int J Climatol 29(8), 790 791 1075-1100. doi: 10.1002/joc.1751 Shongwe ME, van Oldenborgh GJ, van den Hurk B, van Aalst M (2011) Projected changes in 792 mean and extreme precipitation in Africa under global warming. Part II: East Africa. J Clim 793

24(14), 3718-3733. doi: 10.1175/2010JCLI2883.1

794

795	Skamarock WC et al (2008) A description of the Advanced Research WRF version 3. NCAR Tech.
796	Note NCAR/TN-4751STR, 113 pp., doi:10.5065/D68S4MVH.
797	Sun L, Semazzi FH, Giorgi F, Ogallo L (1999) Application of the NCAR regional climate model
798	to eastern Africa: 1. Simulation of the short rains of 1988. J Geophys Res: Atmos 104(D6),
799	6529-6548. doi: 10.1029/1998JD200051
800	Thiery W, Davin EL, Panitz HJ, Demuzere M, Lhermitte S, Van Lipzig N (2015) The impact of
801	the African Great Lakes on the regional climate. J Clim 28(10), 4061-4085. doi:
802	10.1175/JCLI-D-14-00565.1
803	Ummenhofer CC, Sen Gupta A, England MH, Reason CJ (2009) Contributions of Indian Ocean
804	sea surface temperatures to enhanced East African rainfall. J Clim 22(4), 993-1013. doi:
805	10.1175/2008JCLI2493.1
806	Vizy EK, Cook KH (2001) Mechanisms by which Gulf of Guinea and eastern North Atlantic sea
807	surface temperature anomalies can influence African rainfall. J Clim 14(5), 795-821. doi:
808	10.1175/1520-0442(2001)014<0795:MBWGOG>2.0.CO;2
809	Vizy EK, Cook KH (2009) Tropical storm development from African easterly waves in the eastern
810	Atlantic: A comparison of two successive waves using a regional model as part of NASA
811	AMMA 2006. J Atmos Sci 66(11), 3313-3334. doi: 10.1175/2009JAS3064.1
812	Vizy EK, Cook KH (2012) Mid-twenty-first-century changes in extreme events over northern and
813	tropical Africa. J Clim 25(17), 5748-5767. doi: 10.1175/JCLI-D-11-00693.1
814	Vizy EK, Cook KH (2019) Observed relationship between the Turkana low-level jet and boreal
815	summer convection. Clim Dyn 1-22. doi: 10.1007/s00382-019-04769-2

816	Vizy EK, Cook KH, Crétat J, Neupane N (2013) Projections of a wetter Sahel in the twenty-first	
817	century from global and regional models. J Clim 26(13), 4664-4687. doi: 10.1175/JCLI-	
818	D-12-00533.1	
819	Vizy EK, Cook KH, Chimphamba J, McCusker B (2015) Projected changes in Malawi's growing	
820	season. Clim Dyn 45(5-6), 1673-1698. doi: 10.1007/s00382-014-2424-x	
821	Wang T, Lu X, Yang S (2019) Impact of south Indian Ocean Dipole on tropical cyclone genesi	
822	over the South China Sea. Int J Climatol 39(1), 101-111. doi: 10.1002/joc.5785	
823	Wenhaji Ndomeni C, Cattani E, Merino A, Levizzani V (2018) An observational study of the	
824	variability of EA rainfall with respect to sea surface temperature and soil moisture. Q J Roy	
825	Meteorol Soc144, 384-404. doi: 10.1002/qj.3255	
826	Woodhams BJ, Birch CE, Marsham JH, Bain CL, Roberts NM, Boyd DF (2018) What Is the	
827	Added Value of a Convection-Permitting Model for Forecasting Extreme Rainfall over	
828	Tropical East Africa?. Mon Weather Rev 146(9), 2757-2780. doi: 10.1175/MWR-D-17-	
829	0396.1	
830	Yang W, Seager R, Cane MA, Lyon B (2015) The annual cycle of EA precipitation. J Clim 28(6),	
831	2385-2404. doi: 10.1175/JCLI-D-14-00484.1	
832	Zhao Y, Nigam S (2015) The Indian Ocean dipole: a monopole in SST. J Clim 28(1), 3-19. doi:	
833	10.1175/JCLI-D-14-00047.1	

## Table 1. Ensemble descriptions

Ensemble name	SSTs used in ensembles
Control (CTL)	Climatological SSTs
Western Indian Ocean (WIO)	Climatological SSTs + SSTA1
Central Indian Ocean (CIO)	Climatological SSTs + SSTA2
Eastern Indian Ocean (EIO)	Climatological SSTs + SSTA3
Warm-cold Indian Ocean (ALL)	Climatological SSTs + SSTA1 + SSTA2 + SSTA3

## Figure Captions

837

853

854

855

856

857

- Figure 1. (a) Simulation domain and SSTs (K) in the control simulations. (b) Elevation (m) as 838 resolved in the 30-km simulation. Thin black lines indicate country outlines. 839 Figure 2. Climatological (1998-2017) precipitation averaged over October 1- December 15 from 840 (a) PERSIANN, (b) TRMM, (c) CHIRPS, (d) CMORPH, and (e) the control ensemble. Black box 841 denotes the EA analysis domain. Thin black lines indicate country outlines. (f) Daily precipitation 842 smoothed using an 11-day running mean averaged over the EA domain in PERSIANN (black), 843 TRMM (green), CMORPH (purple), CHIRPS (orange), and the control ensemble (red). Units: 844 845 mm/day. Figure 3. 850-hPa wind (vectors; m s<sup>-1</sup>) and specific humidity (shaded; g kg<sup>-1</sup>) averaged over 846 October 1- December 15 in (a) ERAI, (b) JRA-55, and (c) the control ensemble. Cross sections of 847 the zonal wind (m s<sup>-1</sup>) along the equator averaged over October 1- December 15 in (d) ERAI, (e) 848 JRA-55, and (f) the control ensemble. Black dashed lines locate the EA analysis domain. 849 Topography is masked out. 850 Figure 4. (a) Precipitation minus evapotranspiration, (b) moisture advection term, (c) residual term, 851 (d) moisture convergence term, (e) zonal moisture convergences term, and (f) meridional moisture 852
  - Figure 4. (a) Precipitation minus evapotranspiration, (b) moisture advection term, (c) residual term, (d) moisture convergence term, (e) zonal moisture convergences term, and (f) meridional moisture convergence term in the moisture budget [Eq. (1)] averaged over October 1 to December 15 in the control climatology. Unit: mm/day. The black box denotes the EA analysis domain. The black contours show country outlines. (g) (m) are the same as (a) (f), respectively, but using ERAI.

    Figure 5. Correlations of TRMM rainfall averaged over the EA domain with (a) ERAI SSTs and (b) NOAA OI SSTs for the October 1 to December 15 climatology. Only correlations with confidence levels higher than 90% in a two-tailed Student's t-test are shaded. Black dots are the

- locations of maxima of the SSTAs in Figure 5c. Black boxes are averaging regions for western,
- central, and eastern Indian Ocean SSTAs. (c) SSTAs (K) in the perturbation simulations.
- Figure 6. Anomalous precipitation (mm/day) for the (a) WIO, (b) CIO, (c) EIO, and (d) ALL
- simulations for October 1- December 15 climatology. Only areas at or above the 90% confidence
- level are shaded. (e), (f), (g), and (h) are the same as (a), (b), (c) and (d), respectively, but near and
- in the analysis domain. The black contours show country outlines. Black boxes denote the EA
- analysis domain. The percentages of the grid boxes in the EA analysis domain that are associated
- with significantly-changed precipitation is indicated in the upper left of each panel.
- Figure 7. (a) 11-day running mean of precipitation averaged over the western domain (30°-35°E,
- 5°S-5°N) in CTL (black), WIO (dark blue), CIO (light blue), EIO (pink), ALL (red), and the linear
- superposition of the WIO, CIO, and EIO ensembles (green). (b) Same as (a) but averaged over the
- eastern domain (35°-40°E, 5°S-5°N). Unit: mm/day.
- Figure 8. Anomalous (a) precipitation minus evapotranspiration, (b) moisture advection term, (c)
- residual term, (d) moisture convergence term, (e) zonal moisture convergences term, and (f)
- meridional moisture convergence term in the moisture budget [Eq. (1)] for the WIO ensemble
- climatology. Unit: mm/day. Vectors in (d)-(f) are anomalous winds (m s<sup>-1</sup>) at 850 hPa for the WIO
- ensemble climatology. Topography is masked out. Black boxes denote the full EA analysis domain.
- 876 Green lines are the boundaries between western and eastern EA analysis domain.
- Figure 9. Anomalous geopotential heights (shaded; gpm) and winds (vectors; m s<sup>-1</sup>) at 850 hPa in
- the WIO ensemble for October 1- December 15 climatology. The yellow dot shows the location
- of the maximum of SSTAs in the WIO simulations. Topography is masked out.
- Figure 10. Anomalous (a) precipitation minus evapotranspiration, (b) moisture convergence term,
- 881 (c) zonal moisture convergences term, and (d) meridional moisture convergence term in the

anomalous winds (m s<sup>-1</sup>) at 850 hPa for the CIO ensemble climatology. Topography is masked out. 883 Black boxes denote the full EA analysis domain. Green lines are the boundaries between western 884 and eastern EA analysis domain. 885 Figure 11. Anomalous geopotential heights (shaded; gpm) and winds (vectors; m s<sup>-1</sup>) at 850 hPa 886 averaged over October 1 – December 15 in the CIO ensemble. The yellow dot shows the location 887 of the maximum of SSTAs in the CIO simulations. Topography is masked out. 888 Figure 12. Anomalous (a) precipitation term minus evapotranspiration term, (b) moisture 889 convergence term, (c) zonal moisture convergences term, and (d) meridional moisture convergence 890 term in the moisture budget [Eq. (1)] for the EIO ensemble climatology. Unit: mm/day. Vectors in 891 (b)-(d) are anomalous winds (m s<sup>-1</sup>) at 850 hPa for the EIO ensemble climatology. Topography is 892 masked out. Black boxes denote the full EA analysis domain. Green lines are the boundaries 893 between western and eastern EA analysis domain. 894 Figure 13. Anomalous geopotential heights (shaded; gpm) and winds (vectors; m s<sup>-1</sup>) at 850 hPa 895 in the EIO ensemble. The yellow dot shows the location of the minimum of SSTAs in the EIO 896 simulations. Topography is masked out. 897 Figure 14. Anomalous MSE (black), c<sub>p</sub>T (green), and Lq (red) in (a) WIO, (b) CIO, and (c) EIO 898 simulations averaged over western EA domain (30°-35°E, 5°S-5°N) (solid) and eastern EA domain 899 (35°-40°E, 5°S-5°N) (dashed) averaged over October 1 – December 15. Topography is masked 900 out. Unit:  $10^3 \text{ m}^2 \text{ s}^{-1}$ . 901

moisture budget [Eq. (1)] for the CIO ensemble climatology. Unit: mm/day. Vectors in (d)-(f) are

882

902

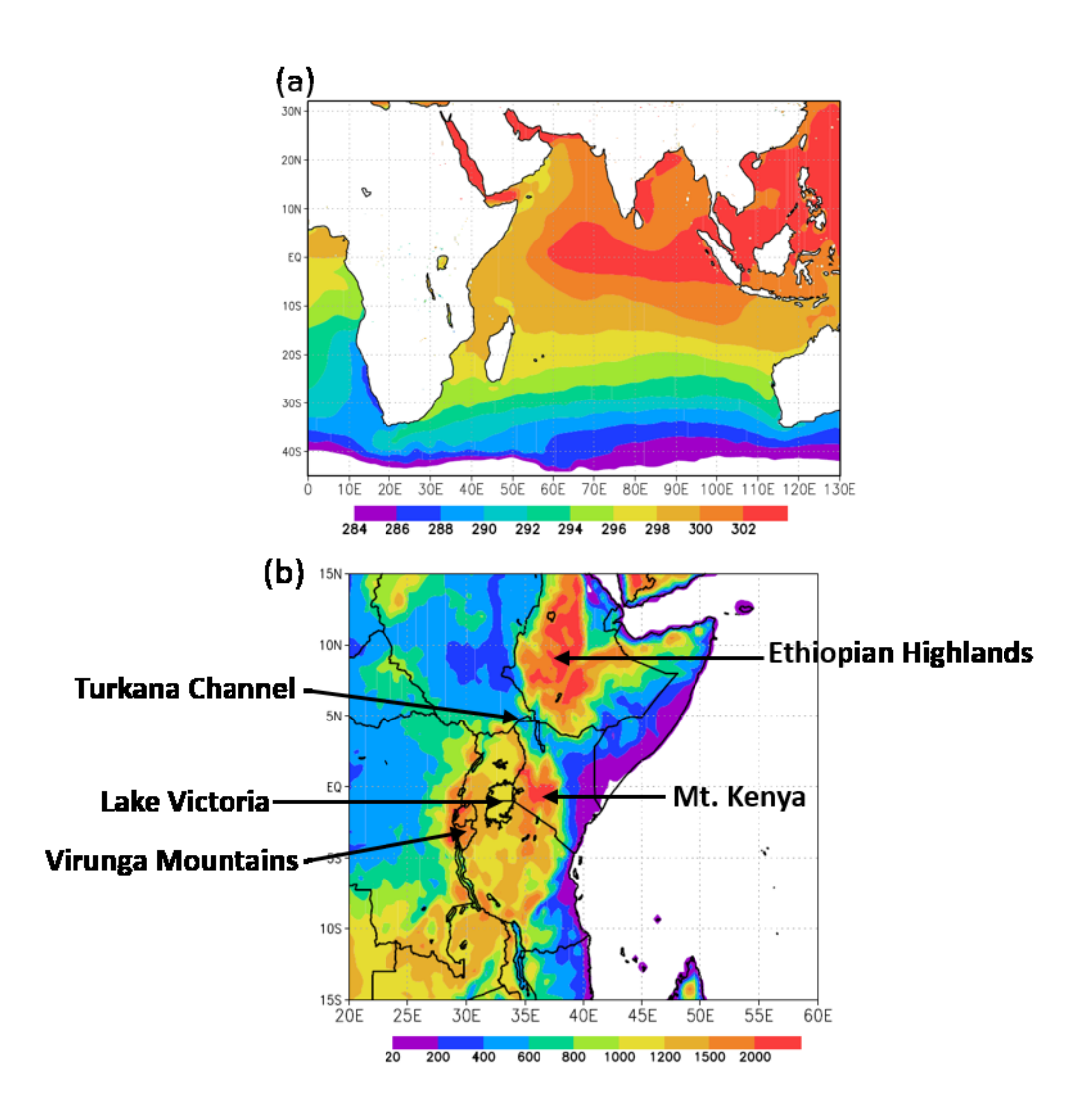


**Figure 1.** (a) Simulation domain and SSTs (K) in the control simulations. (b) Elevation (m) as resolved in the 30-km simulation. Thin black lines indicate country outlines.

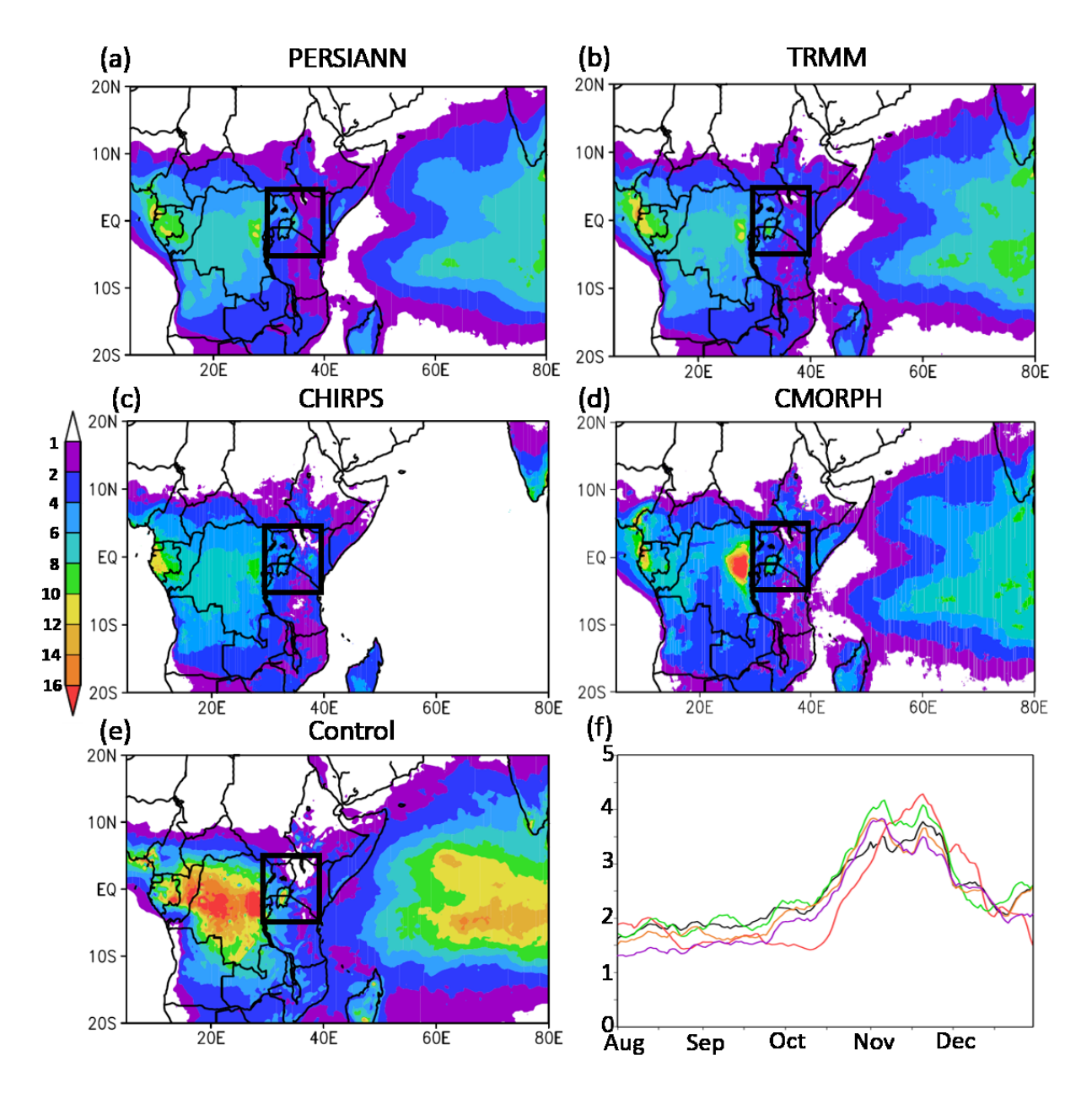


**Figure 2.** Climatological (1998-2017) precipitation averaged over October 1- December 15 from (a) PERSIANN, (b) TRMM, (c) CHIRPS, (d) CMORPH, and (e) the control ensemble. Black box denotes the EA analysis domain. Thin black lines indicate country outlines. (f) Daily precipitation smoothed using an 11-day running mean averaged over the EA domain in PERSIANN (black), TRMM (green), CMORPH (purple), CHIRPS (orange), and the control ensemble (red). Units: mm/day.

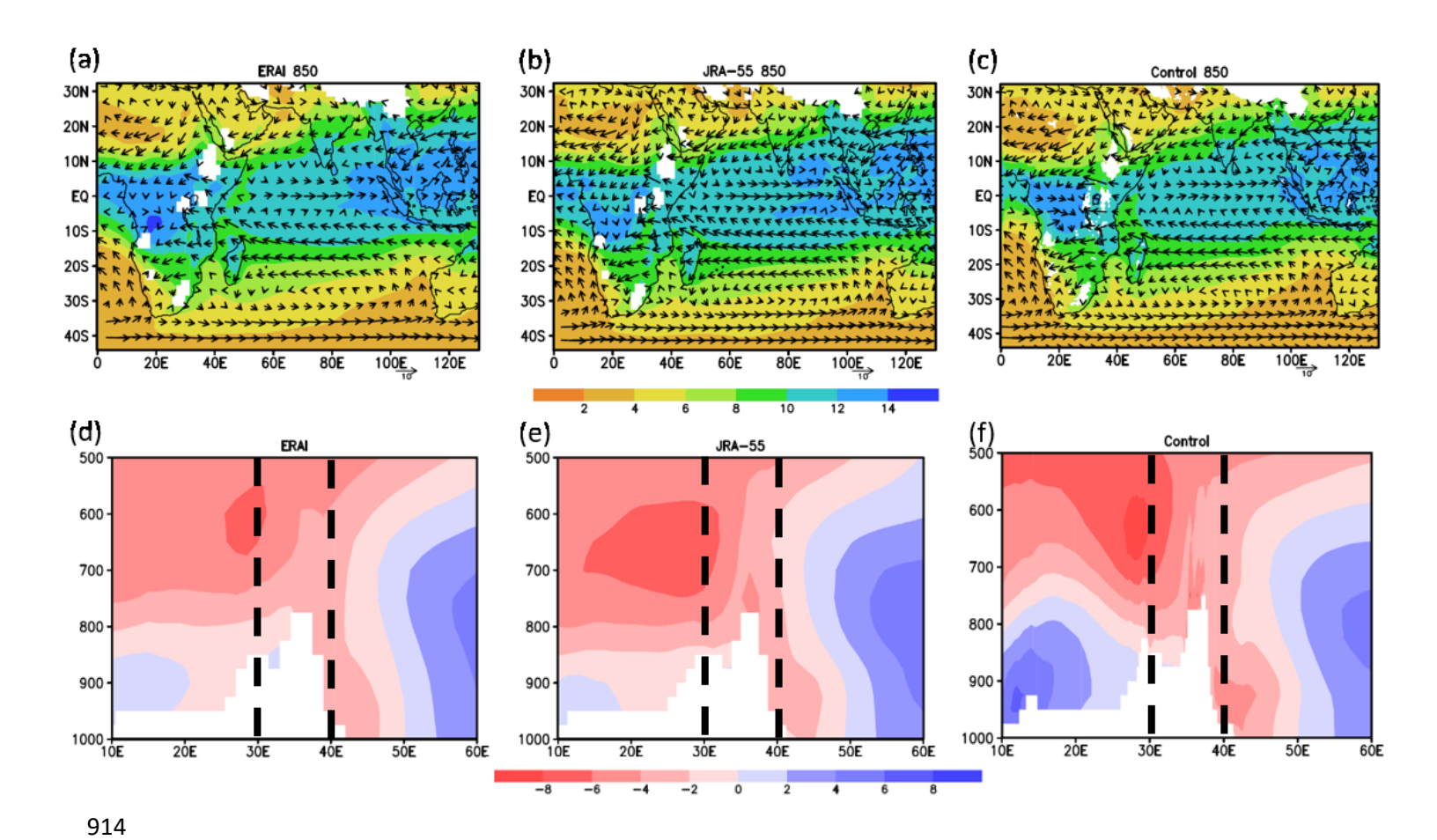


**Figure 3.** 850-hPa wind (vectors; m s<sup>-1</sup>) and specific humidity (shaded; g kg<sup>-1</sup>) averaged over October 1- December 15 in (a) ERAI, (b) JRA-55, and (c) the control ensemble. Cross sections of the zonal wind (m s<sup>-1</sup>) along the equator averaged over October 1- December 15 in (d) ERAI, (e) JRA-55, and (f) the control ensemble. Black dashed lines locate the EA analysis domain. Topography is masked out.

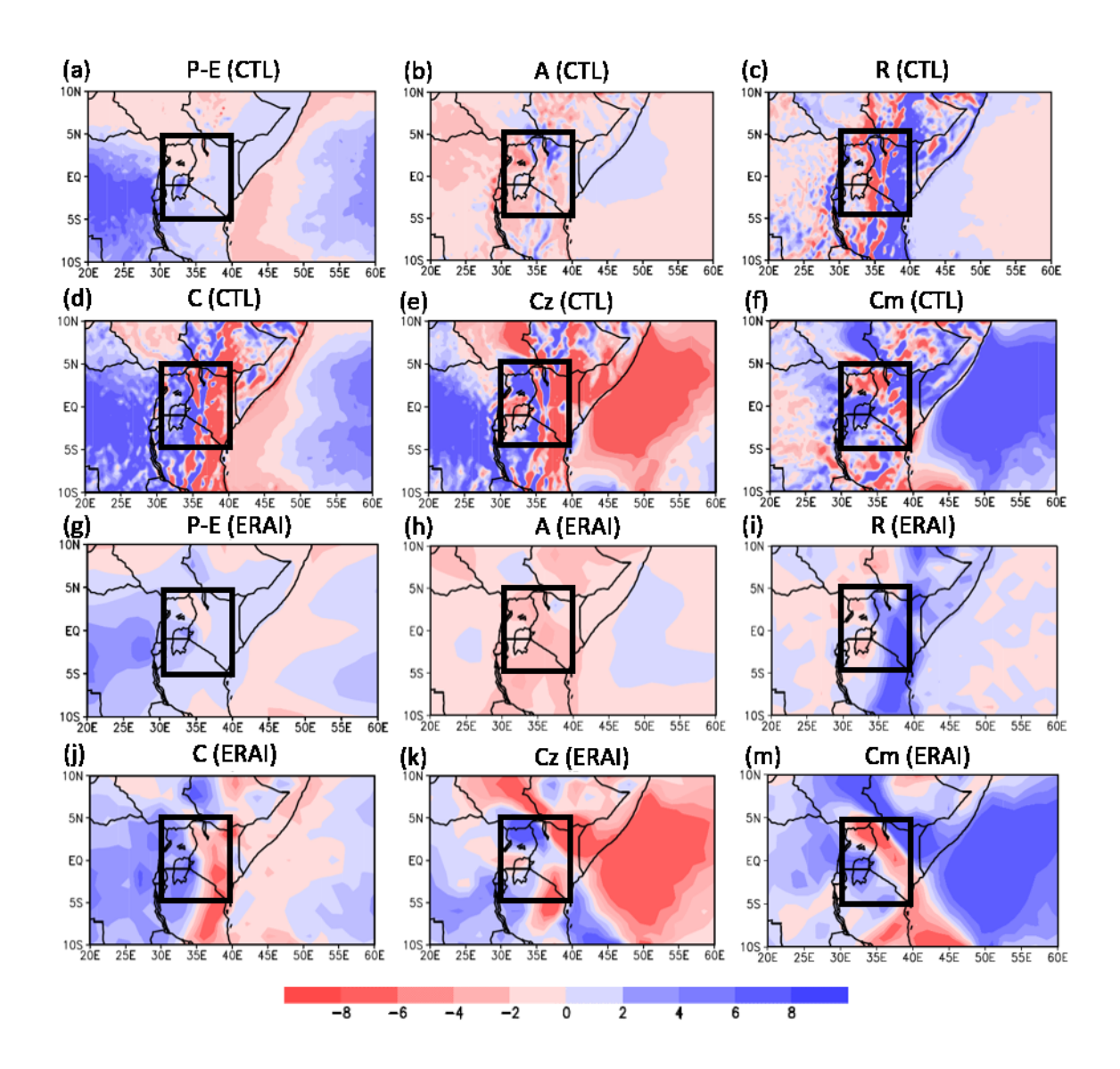


**Figure 4.** (a) Precipitation minus evapotranspiration, (b) moisture advection term, (c) residual term, (d) moisture convergence term, (e) zonal moisture convergences term, and (f) meridional moisture convergence term in the moisture budget [Eq. (1)] averaged over October 1 to December 15 in the control climatology. Unit: mm/day. The black box denotes the EA analysis domain. The black contours show country outlines. (g) - (m) are the same as (a) - (f), respectively, but using ERAI.

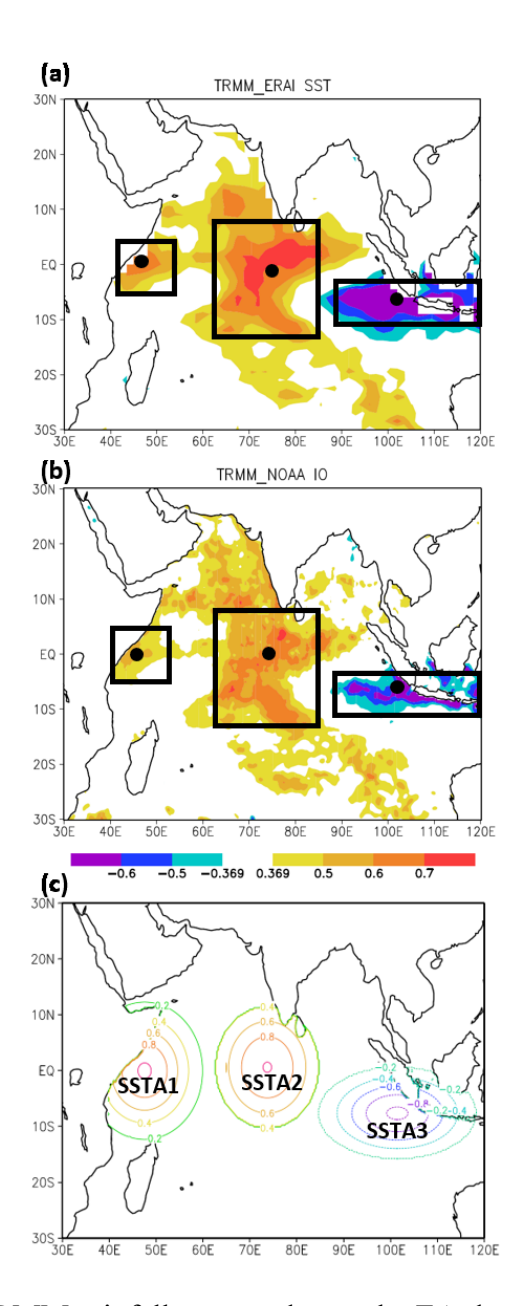


**Figure 5.** Correlations of TRMM rainfall averaged over the EA domain with (a) ERAI SSTs and (b) NOAA OI SSTs for the October 1 to December 15 climatology. Only correlations with confidence levels higher than 90% in a two-tailed Student's t-test are shaded. Black dots are the locations of maxima of the SSTAs in Figure 5c. Black boxes are averaging regions for western, central, and eastern Indian Ocean SSTAs. (c) SSTAs (K) in the perturbation simulations.

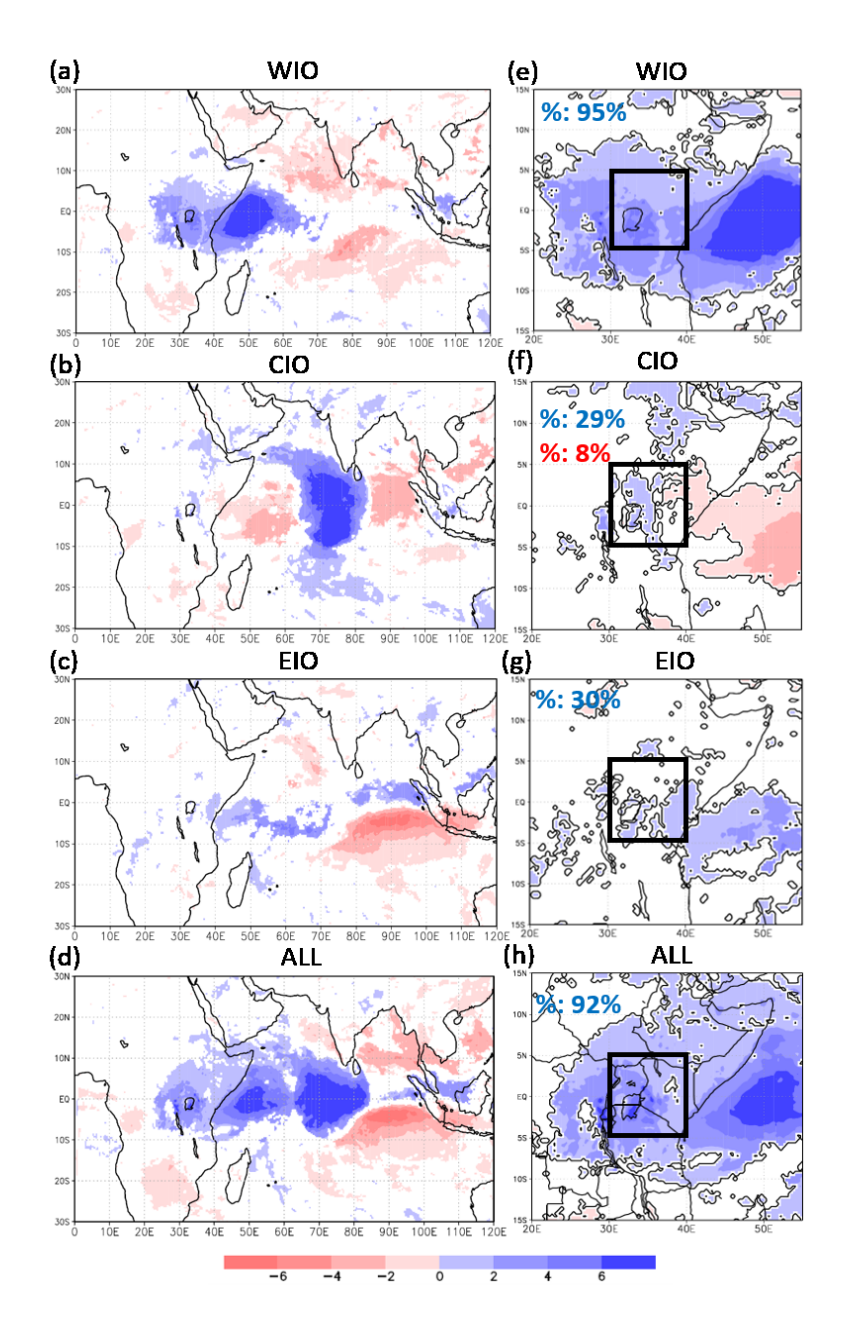


**Figure 6.** Anomalous precipitation (mm/day) for the (a) WIO, (b) CIO, (c) EIO, and (d) ALL simulations for October 1- December 15 climatology. Only areas at or above the 90% confidence level are shaded. (e), (f), (g), and (h) are the same as (a), (b), (c) and (d), respectively, but near and in the analysis domain. The black contours show country outlines. Black boxes denote the EA analysis domain. The percentages of the grid boxes in the EA analysis domain that are associated with significantly-changed precipitation is indicated in the upper left of each panel.

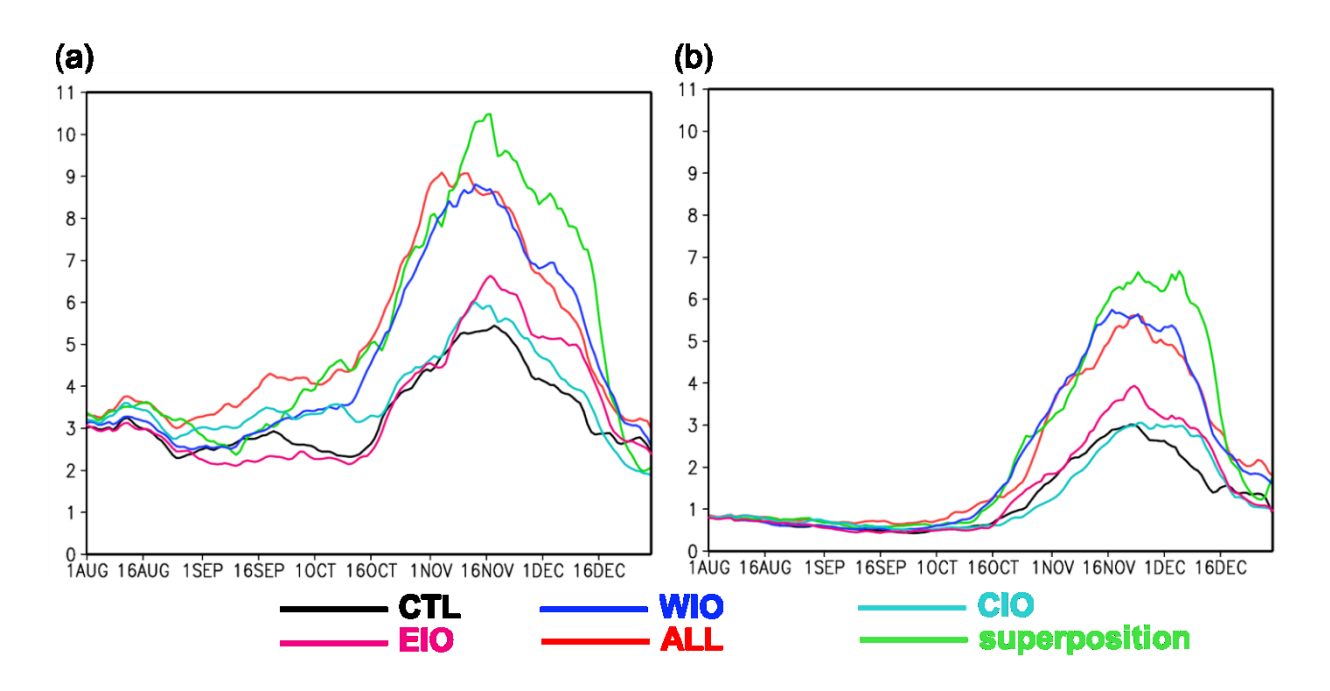


**Figure 7.** (a) 11-day running mean of precipitation averaged over the western domain (30°-35°E, 5°S-5°N) in CTL (black), WIO (dark blue), CIO (light blue), EIO (pink), ALL (red), and the linear superposition of the WIO, CIO, and EIO ensembles (green). (b) Same as (a) but averaged over the eastern domain (35°-40°E, 5°S-5°N). Unit: mm/day.

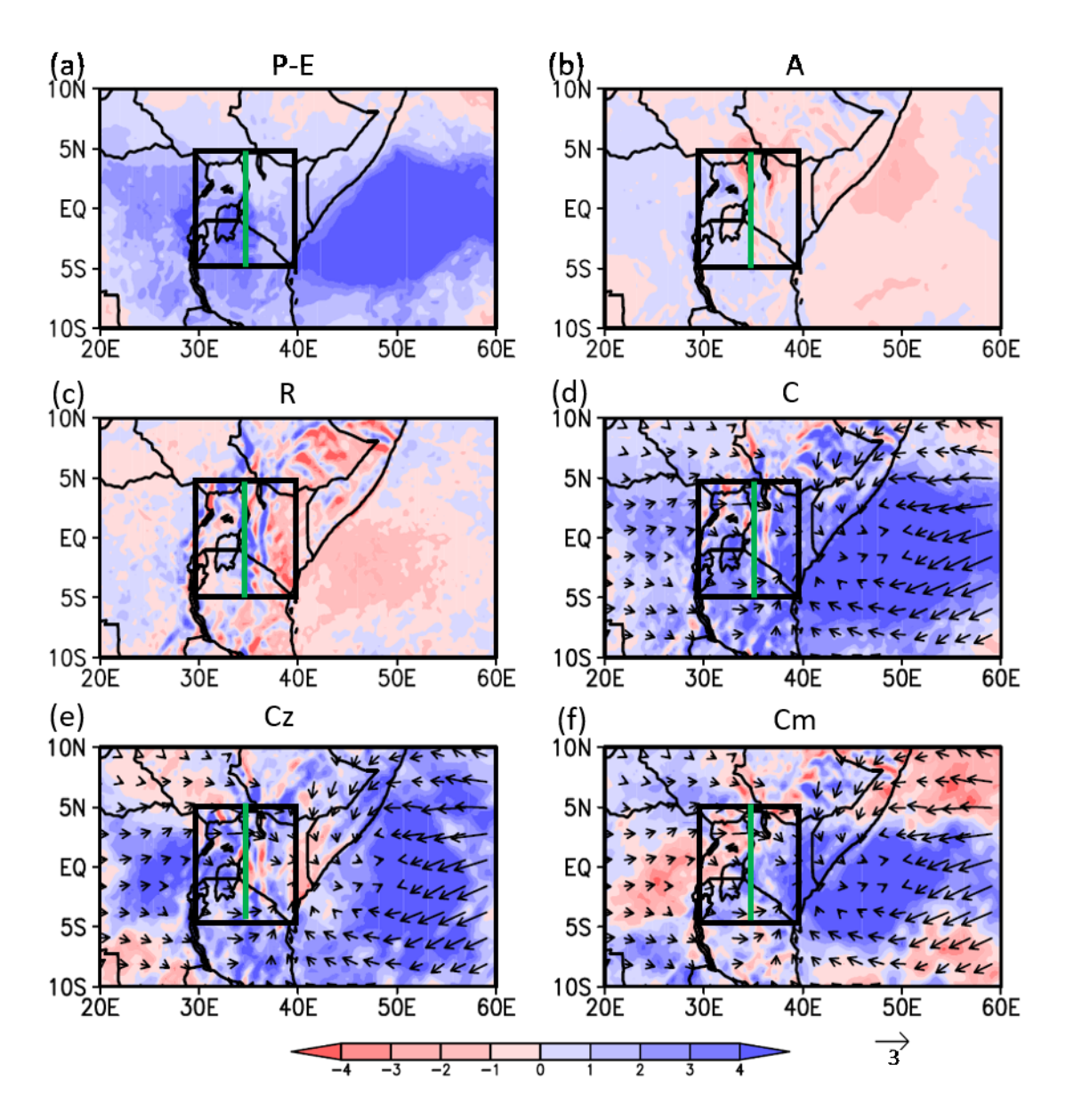


**Figure 8.** Anomalous (a) precipitation minus evapotranspiration, (b) moisture advection term, (c) residual term, (d) moisture convergence term, (e) zonal moisture convergences term, and (f) meridional moisture convergence term in the moisture budget [Eq. (1)] for the WIO ensemble climatology. Unit: mm/day. Vectors in (d)-(f) are anomalous winds (m s<sup>-1</sup>) at 850 hPa for the WIO ensemble climatology. Topography is masked out. Black boxes denote the full EA analysis domain. Green lines are the boundaries between western and eastern EA analysis domain.

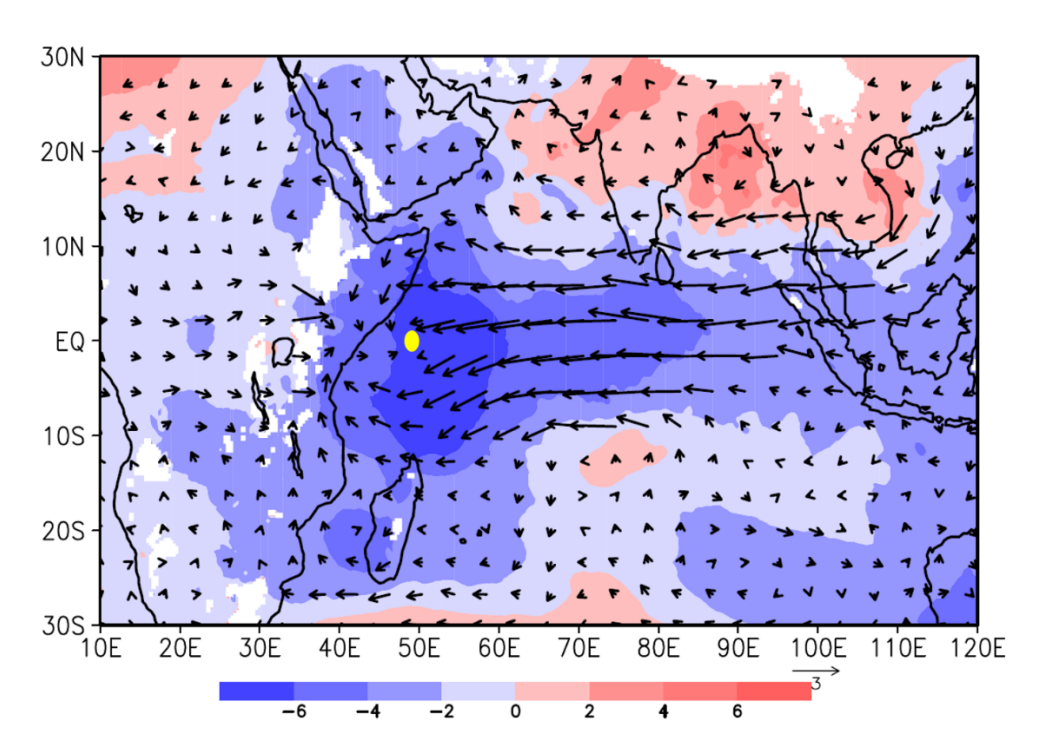


**Figure 9.** Anomalous geopotential heights (shaded; gpm) and winds (vectors; m s<sup>-1</sup>) at 850 hPa in the WIO ensemble for October 1- December 15 climatology. The yellow dot shows the location of the maximum of SSTAs in the WIO simulations. Topography is masked out.

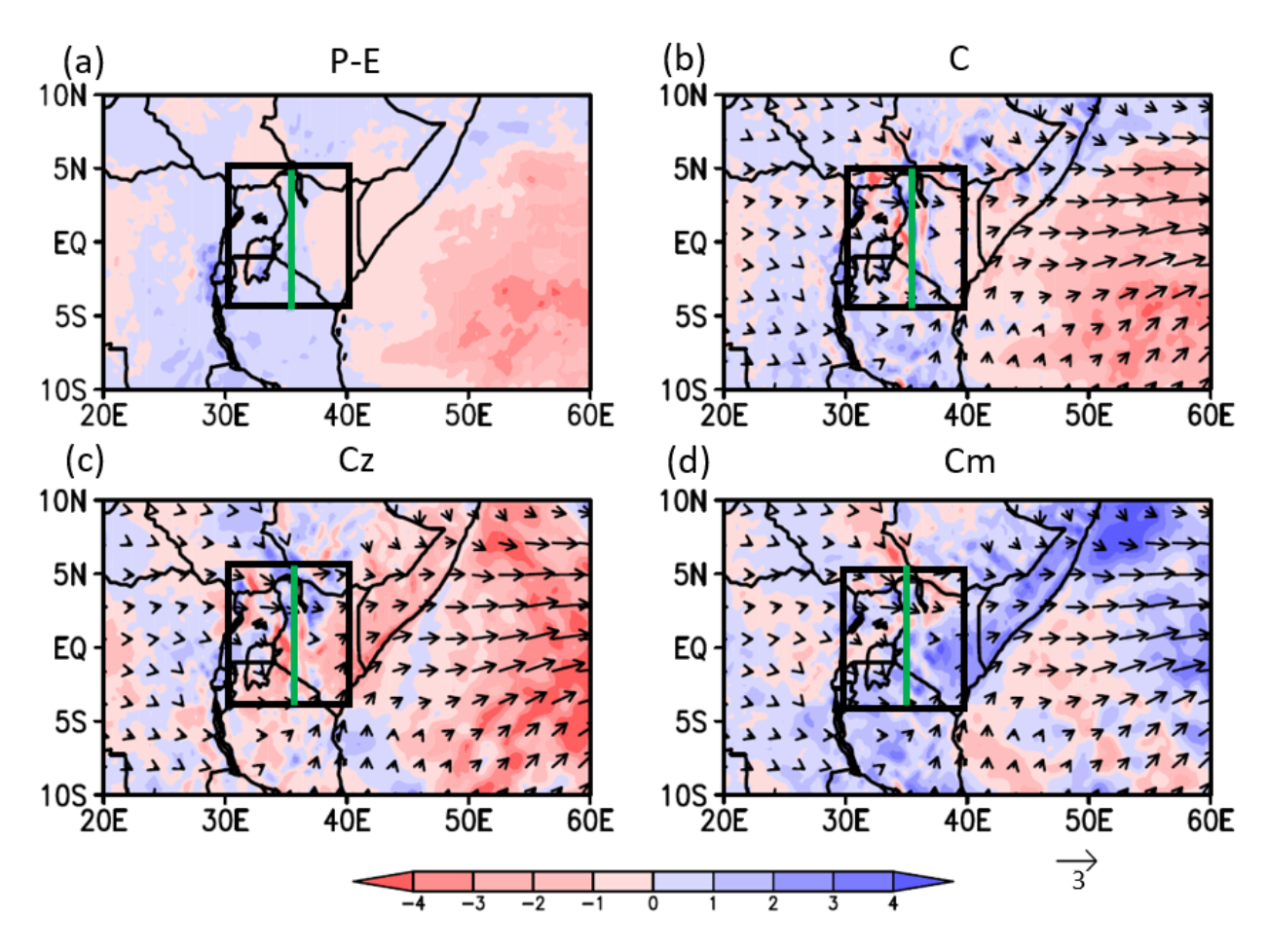


**Figure 10.** Anomalous (a) precipitation minus evapotranspiration, (b) moisture convergence term, (c) zonal moisture convergences term, and (d) meridional moisture convergence term in the moisture budget [Eq. (1)] for the CIO ensemble climatology. Unit: mm/day. Vectors in (d)-(f) are anomalous winds (m s<sup>-1</sup>) at 850 hPa for the CIO ensemble climatology. Topography is masked out. Black boxes denote the full EA analysis domain. Green lines are the boundaries between western and eastern EA analysis domain.

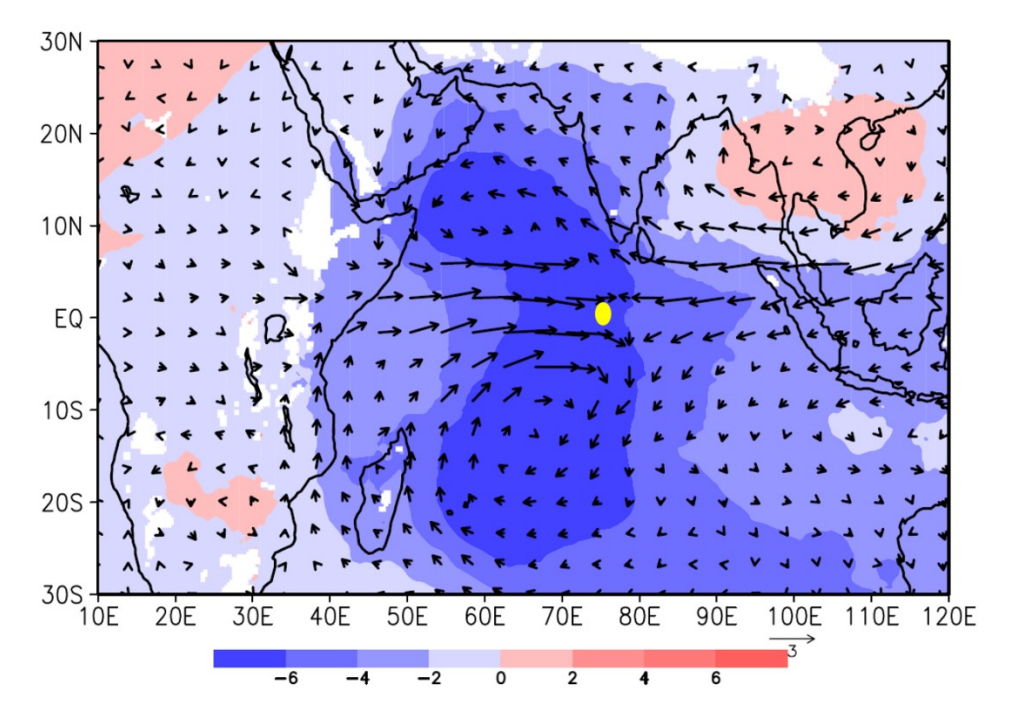


**Figure 11.** Anomalous geopotential heights (shaded; gpm) and winds (vectors; m s<sup>-1</sup>) at 850 hPa averaged over October 1 – December 15 in the CIO ensemble. The yellow dot shows the location of the maximum of SSTAs in the CIO simulations. Topography is masked out.

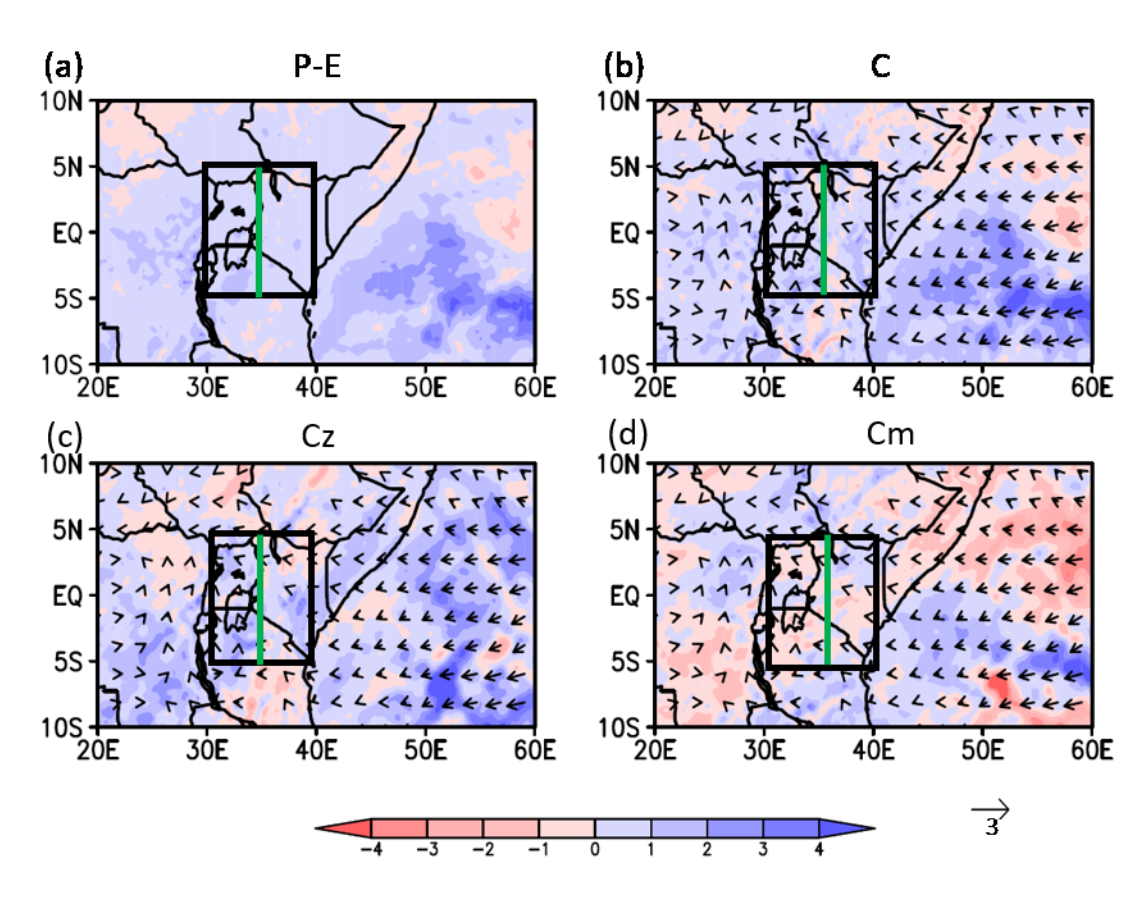


**Figure 12.** Anomalous (a) precipitation term minus evapotranspiration term, (b) moisture convergence term, (c) zonal moisture convergences term, and (d) meridional moisture convergence term in the moisture budget [Eq. (1)] for the EIO ensemble climatology. Unit: mm/day. Vectors in (b)-(d) are anomalous winds (m s<sup>-1</sup>) at 850 hPa for the EIO ensemble climatology. Topography is masked out. Black boxes denote the full EA analysis domain. Green lines are the boundaries between western and eastern EA analysis domain.

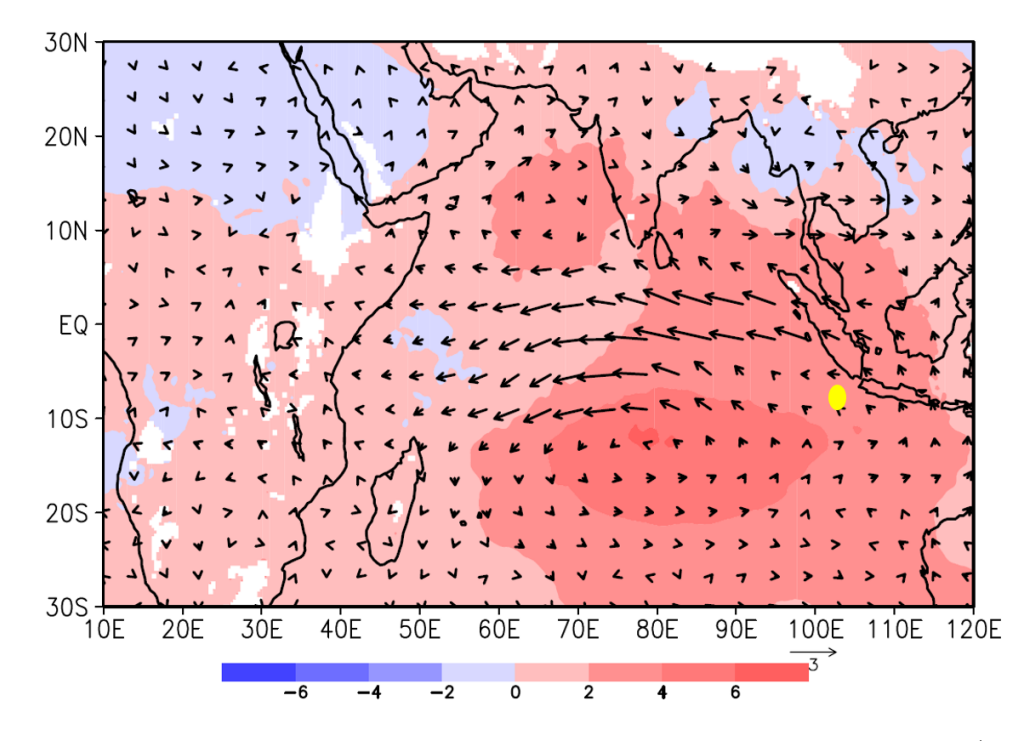


**Figure 13.** Anomalous geopotential heights (shaded; gpm) and winds (vectors; m s<sup>-1</sup>) at 850 hPa in the EIO ensemble. The yellow dot shows the location of the minimum of SSTAs in the EIO simulations. Topography is masked out.

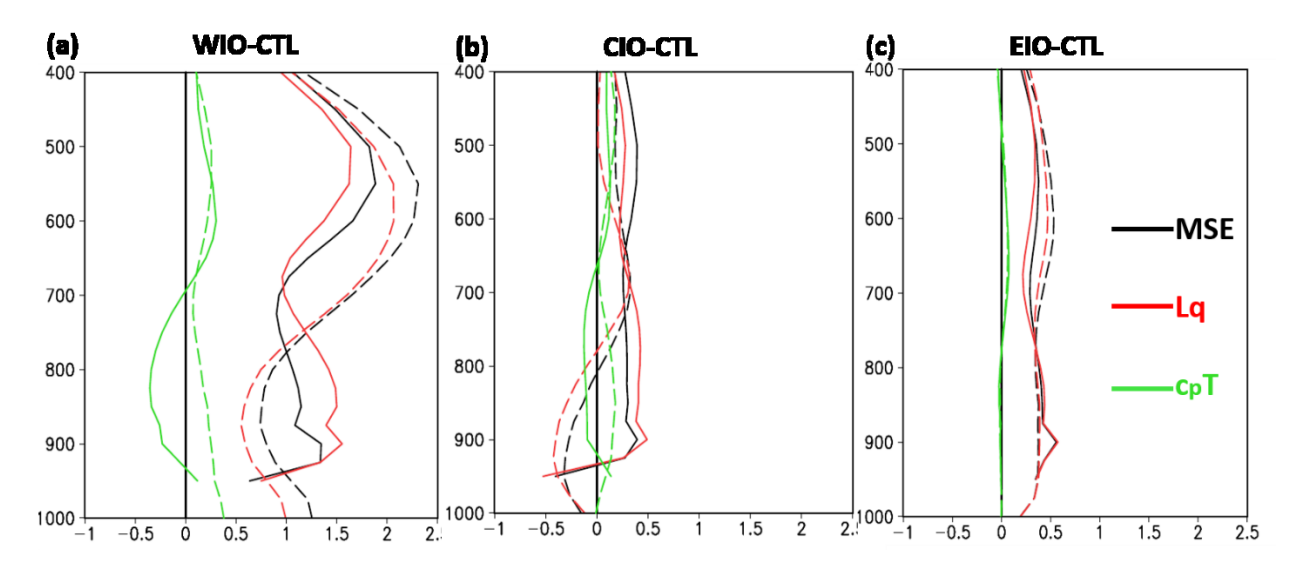


**Figure 14.** Anomalous MSE (black),  $c_pT$  (green), and Lq (red) in (a) WIO, (b) CIO, and (c) EIO simulations averaged over western EA domain (30°-35°E, 5°S-5°N) (solid) and eastern EA domain (35°-40°E, 5°S-5°N) (dashed) averaged over October 1 – December 15. Topography is masked out. Unit:  $10^3$  m<sup>2</sup> s<sup>-1</sup>.